



Preservation and distribution of detrital clay coats in a modern estuarine heterolithic point bar in the Gironde estuary (Bordeaux, France)

Maxime Virolle, Benjamin Brigaud, Hugues Féliès, Raphaël Bourillot, Eric Portier, Patricia Patrier, Hervé Derriennic, Daniel Beaufort

► To cite this version:

Maxime Virolle, Benjamin Brigaud, Hugues Féliès, Raphaël Bourillot, Eric Portier, et al.. Preservation and distribution of detrital clay coats in a modern estuarine heterolithic point bar in the Gironde estuary (Bordeaux, France). *Journal of Sedimentary Research*, 2021, 91 (8), pp.812-832. <10.2110/jsr.2020.146>. <hal-03341573>

HAL Id: hal-03341573

<https://hal.science/hal-03341573v1>

Submitted on 5 Aug 2023

HAL is a multi-disciplinary open access archive for the deposit and dissemination of scientific research documents, whether they are published or not. The documents may come from teaching and research institutions in France or abroad, or from public or private research centers.

L'archive ouverte pluridisciplinaire **HAL**, est destinée au dépôt et à la diffusion de documents scientifiques de niveau recherche, publiés ou non, émanant des établissements d'enseignement et de recherche français ou étrangers, des laboratoires publics ou privés.



HAL Authorization

Preservation and distribution of detrital clay coats in a modern estuarine heterolithic point bar in the Gironde estuary (France)

Maxime Virolle¹, Benjamin Brigaud¹, Hugues Fénies², Raphaël Bourillot², Eric Portier^{1,3}, Patricia Patrier⁴, Hervé Derriennic⁵, Daniel Beaufort⁴

¹Université Paris-Saclay, CNRS, GEOPS, 91405 Orsay, France

²Géoressources et Environnement, ENSEGID, Bordeaux INP, Université Bordeaux Montaigne 33607 Pessac, France

³CV Associés Engineering, 7 chemin de la Marouette, 64100 Bayonne, France

⁴Université de Poitiers, CNRS, UMR 7285 IC2MP, 86073 Poitiers Cedex 9, France

⁵Université Bordeaux, CNRS, UMR 5805 EPOC, 33615 Pessac Cedex, France

Corresponding author: benjamin.brigaud@universite-paris-saclay.fr

ABSTRACT

Estuaries provide an excellent depositional environment to study the interaction between minerals (clays, quartz sands...) and biofilms. The estuary bottom is largely covered by biofilms that impact sediment stability, the mud and clay-coat content in sands, and sedimentary-structure stability, thus influencing sandstone properties during burial. Although numerous oil, gas, and geothermal reservoirs are exploited in estuarine heterolithic point bars, many questions remain about the origin of reservoir properties and heterogeneities in these sedimentary bodies. In order to better understand the sedimentary and microbiologic processes in estuarine systems and to better predict the reservoir quality of estuarine sandstones, this study characterizes a modern heterolithic point bar located in the Garonne estuarine channel at various scales, ranging from the microscopic (thin section)

to the macroscopic (core) scale. Three piston cores 4.5 to 6.8 m long were drilled in the Bordeaux North Point Bar. Three main facies were identified in these cores: (1) sandy gravel; (2) heterolithic, medium-grained sand dunes; and (3) thin heterolithic, fine-grained sand beds with mud drapes. The sands are classified as lithic arkoses to feldspathic litharenites. Detrital clay grain coats, which at deep burial depths are transformed to permeability preserving authigenic chlorite coatings, are observed from the base to the top of the point bar. These detrital clay grain coats are mainly composed of smectite, illite, kaolinite, and chlorite, intermixed with other components, such as diatoms or pyrite. Biofilms of exopolymeric substances (EPSs), mostly produced by diatoms, are believed to control the adhesion of the clay coats to the surface of sand grains. Quantification by thin section shows that on average; about 30% of the sands are coated in the point bar. The proportion of clay-coated grains appears to be independent of facies. Radiocarbon age dating measured on organic matter point to significant vertical mixing, highlighting the significance of erosion and redeposition. The activities of ^{137}Cs and ^{210}Pb indicate a vertical sedimentation rate of *ca.* 0.02 m.yr^{-1} in the muddy chute channel. These ages, coupled to historical maps, suggest that the present-day point bar has developed over the last 300 years with a vertical sedimentation rate ranging from 0.015 to 0.036 m.y^{-1} and a lateral migration rate of about 1 m.y^{-1} . The combination of sedimentary geology, thin-section petrography, and mineralogy at high spatial and temporal resolutions highlights the potential of this study area as a modern analogue for ancient tidally influenced point-bar deposits associated with clay coatings.

Key words: Facies, Sand, Clay coats, Estuary, Point bar, Gironde, Reservoir analogue, Petrography

INTRODUCTION

51 Estuaries provide an excellent depositional environment to study the interaction between
52 minerals (clay coating, quartz sands...) and biofilms, mostly produced by diatoms (Smith and
53 Underwood, 1998; Decho, 2000; Wooldridge et al., 2017a; Virolle et al., 2019a; Duteil et al.,
54 2020). Estuarine biofilms consist of exopolymeric substances (EPSs), composed of
55 polysaccharides, proteins, lipids, and nucleic acids, and reactive groups, such as carboxyl or
56 sulfate (Stoodley et al., 2002; Braissant et al., 2007; Duteil et al., 2020). The reactive groups
57 in EPSs formed in shallow marine and coastal environments adhere to mineral surfaces (e.g.,
58 clays and sands; Duteil et al., 2020), changing the properties of sediments (Malarkey et al.,
59 2015) and also adsorbing metals (Decho, 2000; Pace et al., 2018). The estuary bottom is
60 largely covered by biofilms that influence sediment stability (Decho, 2000; Malarkey et al.,
61 2015; Shchepetkina et al., 2017, 2018). Biofilms and their EPSs may also play a significant
62 role in Precambrian stratigraphy and sedimentary environmental interpretations, influencing
63 both sediment stability and sedimentary-structure stability (Decho, 2000; Sarkar et al., 2005;
64 Malarkey et al., 2015; Shchepetkina et al., 2017, 2018). EPS is believed to support
65 attachment of organisms to the mud sediment and as a protective cocoon to shelter the
66 organisms against desiccation and erosion (Decho, 2000). Many studies show that tidally
67 influenced point-bar deposits form moderate- to high-quality reservoirs (Martinius et al.,
68 2005; Finotello et al., 2018). Common internal depositional features in point-bar reservoirs
69 are lateral-accretion surfaces and associated bedding features that create intermediate-
70 scale heterogeneities (Jordan and Pryor, 1992; Pranter et al., 2007; Cosma et al., 2019; La
71 Croix et al., 2019). Although porosity and permeability in sandstone reservoirs, including
72 tidally influenced point bars in estuaries, could be damaged by quartz overgrowth, it is
73 widely accepted that authigenic clay chlorite coatings help inhibit quartz cement and
74 preserve deep-reservoir quality (Ehrenberg, 1993; Bloch et al., 2002; Worden and Morad,

2003; Saïag et al., 2016; Worden et al., 2020). Recently, clay coats have been documented in modern shallow-marine deposits of estuaries and estuarine channels (Wooldridge et al., 2017b; Griffiths et al., 2018, 2019b, 2019a; Virolle et al., 2019a). These coats appear to have formed by thermally driven transformations of clay-mineral precursors (Aagaard et al., 2000; Haile et al., 2015; Worden et al., 2020). In modern estuarine environments, clay minerals are found in the sediment during or just shortly after deposition, and EPS appears to play an important role in binding detrital clay to sands (Dowey et al., 2017; Jones, 2017; Griffiths et al., 2019b; Wooldridge et al., 2019a; Virolle et al., 2019a; Duteil et al., 2020). These initial detrital clay minerals are believed to initiate chloritization by promoting the formation of clay-mineral precursors (e.g., berthierine) (Beaufort et al., 2015; Virolle et al., 2019b; Worden et al., 2020). Recent studies of modern analogues such as the Ravenglass (United Kingdom), Gironde (France) and Petitcodiac (Canada) estuaries show that tidal bars in the inner estuary and tidal marshes contain well developed detrital clay coats (Shchepetkina et al., 2017, 2018; Griffiths et al., 2018; Wooldridge et al., 2019a; Virolle et al., 2020). However, few studies have focused on documenting the grain-size distribution, mineralogy, presence, and distribution of clay coats in point bars deposited in the estuarine channels up to the fluvial–estuarine transition zone, except for studies on the Ogeechee River (USA) (Shchepetkina et al., 2016a), the Petitcodiac River Estuary (Shchepetkina et al., 2017, 2018), the channel parts of the Ravenglass estuary (Griffiths et al., 2018, 2019b, 2019a) and the Garonne estuarine channel, located in the upstream part of the Gironde estuary (Virolle et al., 2019a). To date, no study has evaluated the influence of point-bar architecture on clay-coat distribution. Therefore, comprehensive models of detrital-clay coating processes, distribution, preservation, and heterogeneity in these challenging heterolithic point bars are still needed.

This study focused on the modern Bordeaux North heterolithic point bar, located in the Garonne estuarine channel (SW France). The objective was to characterize the point-bar heterogeneity from large-scale (i.e., hundreds of meters) to microscale and to discuss the factors potentially influencing clay-grain-coat occurrences and reservoir potential. This primary goal of this study is to provide a better understanding of the distribution and prediction of porosity and permeability in deeply buried tidally influenced sandstone reservoirs.

GEOLOGICAL SETTING

The Gironde estuary (Nouvelle Aquitaine; southwestern France) is one of the largest estuaries in Europe with a surface area of 630 km² (Sottolichio et al., 2011) (Fig. 1A). The estuary is divided into three morphological zones: (1) the Garonne and Dordogne estuarine (meandering) channels, characterized by the deposition of sandy heterolithic point bars; (2) the inner estuary funnel, where the tidal bars of the bay-head delta are deposited; and (3) the outer estuary funnel, consisting in a wide muddy central basin with tidal bars and a large tidal inlet channel at its seaward extremity (Fig. 1A; Allen, 1991; Allen and Posamentier, 1993; Féliès and Tastet, 1998; Billy et al., 2012; Chaumillon et al., 2013; Virolle et al., 2020). The Bordeaux North point bar is located in the Garonne estuarine channel. It is a sinuous single channel, 85 km long, which extends inland from the landward extremity of the estuary funnel to the upstream tidal limit located 160 km from the estuary mouth (Fig. 1A). It is characterized by its low gradient and narrow channel (about 500 m at Bordeaux). Several point bars are observed along the meanders. These point bars are heterolithic and are composed of fluvial sand dunes and amalgamated slack-water mud drapes (Allen, 1991; Virolle et al., 2019a). The Bordeaux North point bar is located 94 km upstream from the

estuary mouth, north of the city of Bordeaux. It is about 1100 m long and 200 m wide (Fig. 1B, C). It has been deposited in the lower part of the intertidal zone, including the entire subtidal zone, down to the thalweg of the channel. The intertidal part of the point bar is covered by (1) a network of small dunes, which can be observed from the low-tide limit to the crest of the bar, and (2) a muddy chute channel, around 100 m wide, located between the crest of the point bar and the channel bank. The channel banks are composed of a 3-m-thick section of muddy estuarine coastal-plain sediments that were deposited up to the high-tide limit. The Garonne river's discharge rate varies seasonally, reaching the highest values in January–February and the lowest in August–September (Coynel et al., 2004). The Gironde is well known for its well-developed Turbidity Maximum Zone (TMZ). In the TMZ, concentration of suspended particle matter (SPM) is reported to be a few g.l^{-1} in surface waters, but in the fluid mud zone (FMZ) near the estuary bottom, the concentration of fine particles ($< 4 \mu\text{m}$) can reach 100–300 g.l^{-1} (Castaing and Allen, 1981; Sottolichio et al., 2011; Etcheber et al., 2011). Jalon-Rojas et al. (2015) reported that the TMZ today in the Garonne channel near Bordeaux seems independent of salinity and density currents.

MATERIAL AND METHODS

This study is mainly based on a new set of shallow piston cores (Fig. 1). Coring was conducted along an east–west transect perpendicular to the long axis of the bar, which has developed almost parallel to the direction of tidal currents. Three cores were drilled in 2016 and 2017 in the heterolithic point bar: 1) Bo-2016-E at the east; 2) Bo-2016-W at the west; and 3) Bo-2017-C in the center of the cross section (Fig. 1C). The length of the cores varies from 4.44 m to 6.70 m. Core spacing is about 60 m (Fig. 1B, C). A portable vibro-corer was used to recover these cores (De Resseguier, 1983) (Fig. 2). During coring, the core barrel is

hammered without any rotation. A fixed piston is maintained with a cable in order to prevent deformation and fluidization due to water escape, thus preserving the delicate sedimentary structures. A reference line indicating the ebb direction of the tide is marked along the entire core section to facilitate orientation of the dune bedding (ebb and flood) after core extraction in the field.

Forty-three plugs (diameter 4 cm) were sampled from the cores. Thin sections of epoxy-impregnated sediment samples were observed under a Nikon Eclipse Ci-POL (Nikon, Tokyo, Japan) and a Leica DM 750P (Leica Microsystems, Wetzlar, Germany) polarizing microscope. Since "clay" may refer to both grain size and mineralogy, this study uses the term "clay fraction" to define the $< 2 \mu\text{m}$ fine-grained sediment (Grim, 1942). In each thin section, the relative surface area (%) of macroporosity and the sediment composition (coated and non-coated quartz grains, feldspars, lithics, pyrite, bioclasts, micas, and clay matrix) were quantified using random grid point counting with JmicroVision Image analysis software (Roduit, 2007). Five grain classes were identified (following the classification defined by Wooldridge et al. (2019b)): (1) absence of clay coats; (2) 1–5% of the grain surface coated; (3) 5–15% of the grain surface coated; (4) 15–30% of the grain surface coated; and (5) more than 30% of the grain surface coated. Scanning electron microscope (SEM) observations, coupled with energy dispersive X-ray spectrometry (EDS), were made on individual sand grains with a Phenom X Pro SEM (Phenom-World B.V., Eindhoven, Netherlands). Cryo-scanning electron microscopy (cryo-SEM) analyses were also conducted on select samples to document EPS and clay minerals attached to the sand grains. Grain size was determined on 78 samples using a Mastersizer 2000 laser granulometer (Malvern, Worcestershire, UK).

170 The relative weight percentage of the clay fraction of homogenized sediment subsamples
171 was also measured on 78 samples. It was expressed as a weight percentage of the sample
172 (wt.%). The compositions of the clay fraction ($< 2 \mu\text{m}$) were determined by X-ray diffraction
173 (XRD) using a PANalytical X'Pert Pro X-ray diffractometer (PANalytical, Almelo, Netherlands).
174 Samples analyzed by XRD analyses included modern mud pebbles in dunes, clay drapes and
175 coats. Semiquantitative estimates of clay minerals (smectite, illite, kaolinite, and chlorite)
176 were made using Macdiff software. These were based on the peak area of the ethylene-
177 glycol diffractograms summed to 100% (the relative error for the peak area is $\pm 5\%$)
178 (Petschick, 2002).

179 Short-wavelength infrared (SWIR) spectroscopy was performed on 318 core samples (103
180 from Bo-2016-E and 215 from Bo-2016-W). Samples for SWIR were collected every 2 cm.

181 Macroscopic fragments of organic matter (wood, leaves, or seed debris) were sampled for
182 radiocarbon dating. The age dating on 27 samples was made using the mass spectrometer
183 accelerator at the Adam Mickiewicz University in Poznań (Poland) and at Paris-Saclay
184 University (Gif-sur-Yvette, France). In all, 228 dried sediment samples from the top 130 cm
185 of core Bo-2016-W were analyzed in 2017 for ^{210}Pb , ^{226}Ra , and ^{137}Cs by direct gamma assay
186 at the Environmental Radioactivity Laboratory at the University of Liverpool (England) using
187 an Ortec HPGe GWL series well-type coaxial-low background intrinsic germanium detector
188 (Appleby et al., 1986). Isotope ^{210}Pb was identified from its gamma emissions at 46.5 keV,
189 and ^{226}Ra by the 295 keV and 352 keV gamma rays emitted by its daughter isotope ^{214}Pb
190 (after three weeks of storage in sealed containers to allow for radioactive equilibration).
191 Isotope ^{137}Cs was measured at 662 keV. Unsupported ^{210}Pb activities were calculated by
192 subtracting ^{226}Ra activity from total ^{210}Pb activity. The absolute efficiencies of the detectors
193 were determined using calibrated sources and sediment samples of known activity. Eight

Corrections were made for the effect of self-absorption of the low energy gamma rays within the sample (Appleby et al., 1992).

Appendix 1 contains the raw XRD values obtained for the clay fraction and raw Image Analysis data on the framework mineralogy of each sample.

RESULTS

Facies Characterization of the Heterolithic Point Bar

Table 1 summarizes the facies descriptions for each point-bar core (from the bottom to top). The sandstones range from lithic arkose to feldspathic arkose (Classification of Folk, 1974) with an average grain composition of quartz (37%), feldspars (11%), lithics (wood debris, soft mud clasts) (14%), carbonates (3%), clays (17%), and micas (5%) (Table 2, Fig. 3A). The average mean grain size in the point-bar deposits is 223 μm . The vertical grain-size profiles show an overall fining-upward trend, ranging from pebbles and coarse-grained sands at the base of the bar (facies F1) to fine-grained sands and mud at the top of the point bar (facies F3). These three facies form the dominant vertical facies association, with F1 at the base to F3 at the top of the heterolithic point bar (Fig. 2). The heterolithic point bar has further been divided into (1) lower point bar (deeper than 3 m below the low water of spring tides), composed mainly of facies F1 and F2, (2) upper point bar, composed mainly of facies F2 and F3, and (3) chute channel deposits composed of the clayey facies F3 only. High resolution photographs of cores are available in Appendices 2, 3, and 4.

Facies F1: Sandy Gravels

Observations: Facies F1 is composed of pluri-centimetric to pluri-decimetric beds of coarse-grained sands, gravels, and lithics (soft mud clasts and organic fragments (wood)), which are

218 bounded by basal erosional surfaces. No sedimentary structures are visible. Locally, horizons
219 rich in organic matter are observed, composed mainly of wood debris, leaves, and seeds. In
220 the channel thalweg at the base of the core, Bo-2016-W, this facies is composed entirely of
221 pebbles (Fig. 4).

222 Interpretation: The coarse-grained deposits of facies F1 are believed to have been deposited
223 during floods stage, when current velocities are highest, whereas the organic-matter debris
224 was deposited during waning flood currents. The pebble bed observed at the base of core
225 Bo-2016-W is interpreted as the upper part of a channel lag deposit.

226

227 **Facies F2: Heterolithic medium-grained sand dunes**

228 Observations: Facies F2 is heterolithic. It is made up of decimeter-thick beds of sand dunes,
229 interbedded with centimeter- to decimeter-thick muddy beds. The sand beds are composed
230 of small- to medium-size dunes (preserved dune set height: 10–30 cm). Their foresets and
231 bottomsets are underlined by mud pebbles and mud drapes. The mud pebbles are
232 subrounded and centimeters thick; mud drapes are a few millimeters thick on the foresets,
233 but up to half a centimeter thick in the bottomsets of the dunes, where they appear to be
234 amalgamated (Fig. 2). Mud-drape couplets (Visser, 1980; Féliès et al., 1999) are preserved in
235 the dune foresets and bottomsets. The bidirectionality of tidal currents can be observed at
236 the dune scale with: (i) flood- and ebb-oriented tidal bundles on dune foresets; and (ii)
237 reactivation surfaces (De Mowbray and Visser, 1984) generated by the subordinate currents,
238 which have eroded the dominant current bundle. Muddy beds are composed of
239 amalgamated millimeter to centimeter-thick individual mud drapes. No bioturbation was
240 observed.

Interpretation: The internal stratification of the sand dunes proves that they were deposited by bidirectional tidal currents, whose velocities exceeded the dune migration threshold. The mud drapes were deposited during slack-water periods in very turbid waters. The apparent lack of bioturbation is typical for estuarine high-turbidity fresh-water estuarine deposits (La Croix et al., 2015).

- **Facies F3: Heterolithic fine-grained sands beds and mud drapes**

Observations: Facies F3 is heterolithic and consists of thin fine-grained sand beds (mostly ripples and linsen), interbedded with centimeter-thick mud layers composed of amalgamated, millimeter-thick individual mud drapes. This facies is characterized by its classic lenticular bedding. Neap-spring-cycle deposits (Boersma and Terwindt, 1981) a few decimeters thick have also been described. The spring-tide deposits consist of centimeter-thick, fine-grained sandy ripples interbedded with thin mud drapes. The neap tide deposits consist of fine-grained silty linsen interbedded with thicker mud drapes. These deposits have been previously described by Musial et al. (2012).

A subfacies of facies F3 is the chute channel deposits, which are located on the western side of the point bar, between the crest of the point bar and the estuarine bank (see core Bo-2016-W location in Fig. 1C and Fig. 2). The chute channel deposits are 3 m thick (Fig. 4). They are characterized by alternating beds of fluid mud (centimeters to decimeters thick) and beds of fine-grained thin sand ripples, linsen, and mud drapes (decimeters thick). A few beds of coarse-grained sand and pebbles (centimeters thick) are occasionally observed.

Rare bioturbation was observed on the surfaces of the mud drapes, generated by millimetric-size small horizontal burrowing worms.

Interpretation: The ripples and linsen were deposited by tidal currents, whose velocities only just exceeded the ripple migration threshold. The thick mud drapes were deposited in highly turbid waters, during long slack-water periods. The preservation of neap-spring-cycle deposits indicates a very high rate of sedimentation with sufficient accommodation space. The subfacies F3 chute-channel deposits are representative: (1) periods of very low current velocities during which the fluid mud layers were deposited, or (2) periods of very high current velocities, attained during high flood stage, resulting in the deposit of coarse-grained sand and pebbles beds [were deposited] in the chute channel. The crypto-bioturbation present at the surface of the chute channel is typical of estuarine high-turbidity fresh-water estuaries.

- **Facies F4: Admixed sand and mud facies**

Observations: Facies F4 was encountered only in core Bo-2016-E, from the surface of the point bar to a depth of 235 cm (Table 1, Fig. 4). It is a mixture of mud and sand, characterized by very disturbed bedding with a lot of brick and shipyard bolts debris.

Interpretation: Facies F4 is made up of anthropized dredging deposits. This facies is confined to a small area on the western side of the point bar.

Contribution of Radiometric Age Datings

- **¹⁴C Datings**

Twenty-one ¹⁴C dates were obtained on the three cores (Bo-2016-W; Bo-2017-C; Bo-2016-E). Results revealed very heterogeneous ages, ranging from 6,280 years before present (BP) to the present (Fig. 4). Except for two ages older than 1,000 years BP, the predominant ages in

the upper part of the tidal bar (between 0 and 4.5 m below the low-water spring-tide level (LWST)) are younger than 400 years BP.

- ²¹⁰Pb Activity

The results of ²¹⁰Pb analyses conducted on core Bo-2016-W are given in Table 3 and figure 5A. Total ²¹⁰Pb activity significantly exceeds that of the supporting ²²⁶Ra in samples down to a depth of around 90 cm. Unsupported ²¹⁰Pb concentrations are very low, with a maximum value of just 38 Bq kg⁻¹. The total ²¹⁰Pb activity exhibits some variation with depth. Between the surface and 50 cm depth, the total activity fluctuates between 45 and 80 Bq kg⁻¹. From 50 to 110 cm deep, it decreases steadily from 70 to 20 Bq kg⁻¹ before stabilizing around 40 Bq kg⁻¹ between 110 cm and 140 cm deep (Fig. 5A).

- ¹³⁷Cs Activity

The ¹³⁷Cs analyses obtained from core Bo-2016-W is around 6000 Bq m⁻². ¹³⁷Cs activity in this core has a well-defined peak at a depth of 28 cm (Table 3, Fig. 5A), reaching a maximum value of 8.4 Bq kg⁻¹. Between 28 to 110 cm, activity fluctuates between 4 and 6 Bq kg⁻¹. A last peak at 5.7 Bq kg⁻¹ is observed at 108 cm depth, before it decreases to almost 0 Bq kg⁻¹ from 116 to 234 cm deep (Table 3). Between the surface sample and 28 cm deep, ¹³⁷Cs activity ranges from almost 2 to more than 8 Bq kg⁻¹.

Characterization of Detrital-Clay Grain Coat

Detrital-clay grain coats are present throughout the heterolithic point bar (down to *ca.* 7 m deep). Clay grain coats were observed around various framework grains (quartz, micas, feldspars, and lithics, except the Channel lag facies F1; Figs. 3B-G). The detrital-clay grain

coats are mainly composed of clay minerals with minor amounts of silt-size quartz grains, coccoliths, diatoms, and framboidal pyrite (Fig. 3F-H). Both optical microscopy and SEM observations show that diatoms are embedded in the detrital clay grain coats from the surface to several meters below the tops of the cores (Figs. 6A-E).

Various textures were observed, ranging from (1) continuous to discontinuous clay drapes, 5 to 50 μm thick, partially to totally cover the surface of the detrital grains (Fig. 3E); (2) aggregates of detrital-clay coats in aggregates scattered on the surface of sand grains (Figs. 3D, 3F); (3) detrital-clay bridges between sand grains (Fig. 3C); to (4) detrital-clay ridges where the clay minerals are oriented at high angles to the surfaces of detrital sand grains. The detrital-clay grain coats are typically less than 1 millimeter thick, ranging mainly from 10 to several hundred μm . All these clay coat textures were observed in all facies (Fig. 3).

Detrital sand grains on average represent 70% of the sample composition, and 31% of the grains are coated (Table 2, Fig. 7). Vertically, the total number of coated grains ranges from 19% to 48% (Table 2; Fig. 8). In each facies, the coated grain-content is very homogeneous: sandy gravel facies (F1) = 29%; heterolithic, medium-grained sand dune facies (F2) = 31%, and heterolithic, fine-grained sand bed and mud drape facies (F3) = 32% (Fig. 7, Table 2). Coat coverage is relatively homogeneous for all cores (Fig. 9). For the finer sand of the heterolithic facies (F3), the two predominant classes of clay grain-coat-coverage are 5–15% and 15–30%. In facies F1 and F2, more than 20% of the grain are coated, with a coverage ranging from 1 to 15% (Fig. 7). Overall, there is no correlation between clay fraction and the percentage of coated grain (Fig. 9A, B).

Characterizations of Clay Fractions and Clay Assemblages

334 The clay fraction is related to the amount of muddy deposits (muddy layers or clay drapes)
 335 and coats in a sample. On average, the total clay content makes up about 20 wt.% of the
 336 sample (Table 2; Figs 8, 9B). In facies F1 and F2, the amount of clay is very consistent (18%),
 337 but it is slightly higher in facies F3 (25%) (Fig. 9B). The muddy chute-channel subfacies (F3)
 338 has a higher clay content (38 wt.%), as shown in Figs. 8 and 9B (Table 2). It should be noted
 339 that the clay-fraction content in facies F3 might be slightly underestimated because of bias
 340 in sample selection (most of the samples were extracted from sandy ripples).
 341 Based on XRD analysis, the clay-mineral assemblage is composed of four main clay minerals:
 342 chlorite, illite, kaolinite, and smectite (Fig. 10, Table 2). Chlorite is characterized by
 343 diffraction peaks at 14.10 Å (001), 7.05 Å (002), 4.73 Å (003), and 3.54 Å (004). The illite
 344 diffraction pattern exhibits diffraction peaks around 9.99 Å (001), 4.99 Å (002), and 3.33 Å
 345 (003). Kaolinite displays a (001) diffraction peak at 7.16 Å and a (002) diffraction peak at 3.57
 346 Å. Smectite is identifiable after ethylene-glycol saturation, with a (001) diffraction peak close
 347 to 17 Å. Smectite is mainly dioctahedral smectite (Latouche, 1971). Smectite (7%) and illite
 348 (8%) have the highest surface areas (on the diffractogram), while chlorite and kaolinite have
 349 a much lower surface area (average of 2%; Fig. 9C-F, Table 2). Clay assemblages are relatively
 350 homogeneous between facies, except for facies F3 in core Bo-2016-W (the muddy chute-
 351 channel subfacies) where the abundance of all clay minerals is systematically higher:
 352 smectite (14%), illite (16%), kaolinite (4%), and chlorite (3%) (Fig. 9C-F).
 353 Short-wavelength infrared (SWIR) measurements were made along cores Bo-2016-W and
 354 Bo-2016-E. Of particular interest were three bands: (1) the water-absorption band, which
 355 can be correlated with the presence of swelling minerals such as smectite, and (2) the 2200
 356 cm^{-1} (Al_2OH) and 2253 cm^{-1} bands, both of which mainly characterize aluminous phases, such
 357 as micas or clay minerals. In core Bo-2016-E, none of the bands show significant variation

with depth or even between facies in core Bo-2016-E (Fig. 8). In core Bo-2016-W, each of the three bands displays a slightly increasing trend with depth, coupled with higher fluctuations (Fig. 8).

DISCUSSION

Age Model of Cores

Previous studies have used ^{137}Cs – ^{210}Pb chronologies to reconstruct the morphological evolution of point-bar deposits through time (D'Alpaos et al., 2017). In montmorillonite, vermiculite, kaolinite, and illite, the isotope ^{137}Cs is essentially fixed on particles of permanent charge due to cationic exchange on the mineral compounds (Grousset et al., 1999). The isotope ^{137}Cs is mostly incorporated into the illitic clay matrix of the Gironde suspended matter and is therefore difficult to desorb. This is why it was relevant to carry out ^{137}Cs – ^{210}Pb dating in the muddy deposits of the chute channel enriched in smectite (montmorillonite) and illite (Fig. 5A). Calibrations were made by comparisons with Grousset et al. (1999) and Jouanneau et al. (1999), who studied a core located 3 km upstream in the flood-tide dock of Bordeaux (Fig. 1B).

The atmospheric initiation of radioactive fallout since 1952 is responsible for the increase in ^{137}Cs activity in sediments, reaching a ^{137}Cs peak in 1964 (e.g., Monna et al., 1999; Evrard et al., 2020). The beginning of this increase can be seen at *ca.* 124 cm with a small ^{137}Cs peak at 0.4 Bq kg⁻¹ (Fig. 5A, B). The peak of ^{137}Cs activity at 5.7 Bq kg⁻¹ recorded at 108 cm below the top of core could correspond to the year 1964, which was marked by the maximum impact of nuclear tests in the northern hemisphere (Pourchet et al., 1989; Williams and Hamilton, 1995; Jouanneau et al., 1999; Monna et al., 1999) (Fig. 5A, B). This increase in ^{137}Cs activity from the mid-1950s to 1964, also corresponds to an increase in cadmium (Cd) in the estuary,

suggesting an increase in river inputs (Grousset et al., 1999; Jouanneau et al., 1999). In the Bordeaux dock core, ^{137}Cs reaches a maximum at 3 dpm g⁻¹ (50 Bq kg⁻¹) for 1964 (Jouanneau et al., 1999), whereas ^{137}Cs reaches 120 Bq kg⁻¹ in Lake Geneva (Switzerland) for the same year (Monna et al., 1999). The presence of small but significant concentrations of ^{137}Cs down to a depth of 110 cm suggests that all sediments above this depth postdate the large-scale release of this artificial radionuclide into the global environment from the mid-1950s onwards (Fig. 5A-B). This is consistent with the suggestion that the greatest depth (~90 cm) at which significant amounts of unsupported ^{210}Pb could be detected was likely to span at most 2–3 ^{210}Pb half-lives (40–60 years). According to the age model of the core from the dock of Bordeaux, a second ^{137}Cs peak occurs in the 1970s (Grousset et al., 1999). The peak found at 84 cm (5.7 Bq kg⁻¹) in core Bo-2016-W (Fig. 5A-B) could also correspond to this event.

The third ^{137}Cs peak (ca. 20 Bq kg⁻¹) recognized in the Bordeaux dock core corresponds to the Chernobyl accident that occurred in 1986 (Grousset et al., 1999). The third peak (6.5 Bq kg⁻¹) is also found 60 cm deep in core Bo-2016-W (Fig. 5A-B). The fourth ^{137}Cs peak (8.4 Bq kg⁻¹) found at 28 cm is not attributed to a known discharge, source or event. The temporal evolution of ^{210}Pb element is characterized by great variability in the upper part of the chute channel between 20 and 30 cm, possibly suggesting sediment remobilization (Fig. 5A).

Placing year 1964 at 108 cm and 1986 at 60 cm, the average sedimentation rate can be estimated to be ca. 2 cm.y⁻¹ (Fig. 5C). The results from ^{210}Pb total activity are consistent with ^{137}Cs activity, as the first 110 centimeters of the core would be less than 60 years old (Fig. 5A, B). By anchoring years 1964 at 108 cm and 1986 at 60 cm, and applying a sedimentation rate of 2 cm y⁻¹, the sample at 12 cm which contains significantly higher concentrations of

uranium-series radionuclides appears to have been deposited to around 2010. The samples at 26–28 cm contained the highest ^{137}Cs concentration, suggesting that they were deposited around 2002.

Radiocarbon ages dating was performed on the three cores at all depths. These ages are very heterogeneous, ranging from 6280 ± 30 years BP to modern (Fig. 4). Results may depend on the nature of organic remains. Fine organic debris, such as leaves and twigs, are assumed to record ages close to the age of sediment deposition (because they are seasonally produced and readily decomposed (Kochel and Baker, 1988; Webb et al., 1988) and therefore are believed to yield the most accurate ^{14}C dates in fluvial deposits (Ely et al., 1992). Detrital wood and charcoal ^{14}C ages may predate fluvial deposits by centuries after sedimentation and can be remobilized giving erroneous ages of deposition (Long and Rippeteau, 1974; Blong and Gillespie, 1978; Ely et al., 1992). In the Bordeaux North point bar, radiocarbon ages measured on seeds and leaf debris are younger than 400 years (Fig. 4). The top 110 cm of the well-calibrated core Bo-2016-W, yielded two ^{14}C ages (modern and 195 ± 30 years BP). This suggests that the youngest age obtained provides information about sediment age. Older ^{14}C ages suggest that old organic matter has been remobilized and transported into the estuary (Virolle et al., 2020). In core Bo-2016-W, an age of 70 ± 30 years BP was obtained at a depth of 3.1 m (in the upper section of the point bar) (Fig. 4), suggesting that the top 3 m is relatively young, probably deposited during the last century. This suggests a sedimentation rate of *ca.* 3 cm y^{-1} . In core Bo-2016-W, an age of 355 ± 30 years BP at a depth of 5.3 m suggests that the sedimentation rate for the top 5 m was around 1.5 cm y^{-1} . In core Bo-2017-C, leaf fragments at a depth of 3.2 m yielded an age of 170 ± 20 years BP at the top of the lower point bar (Fig. 4). This age suggests that the top 3 m was also relatively young, probably deposited in the two last centuries, and

corresponding to a sedimentation rate of *ca.* 1.9 cm y⁻¹. In core Bo-2016-E, the age 95 ± 30 years BP in the lower point bar (depth of 3.4 m) (Fig. 4) suggests a sedimentation rate of 3.6 cm y⁻¹ in the upper point bar. A recent study reports that the sedimentation rate is about 1–3 mm.y⁻¹ in a tidal point bar of the lagoon of Venice (Donnici et al., 2017). The sedimentation rate in the Bordeaux point bar is higher by a factor of ten.

Radiometric ages (¹⁴C, ¹³⁷Cs, and ²¹⁰Pb) suggest that the formation of the Bordeaux North point bar is relatively young and rapid (< 300 years). This is consistent with lateral migration studies which document that the point bar has migrated about 200 m since the period 1820–1866, yielding a lateral-accretion rate of 1 m.y⁻¹ (Fig. 11). In comparison, detailed studies of the tidal point bars of the Venice Lagoon show lateral-accretion rates of only 0.1 to 0.25m.y⁻¹ (Donnici et al., 2017; D’Alpaos et al., 2017; Ghinassi et al., 2018).

Origin of Detrital-Clay Grain Coats

Grain coats observed in the Gironde estuary are mainly composed of clay minerals (Fig. 6). As described in Virolle et al. (2019a), these clay minerals are detrital and supplied by the Garonne and Dordogne rivers. These two rivers are responsible for 70% and 18%, respectively, of the supply of detrital clay minerals to the estuary funnel respectively (Latouche, 1971; Parra et al., 1998). The seasonal position of the turbidity-maximum zone (TMZ) seems to be a major factor controlling the amount of clay, the clay-mineral assemblage, and the coated-grain distribution, in the intertidal zone of the estuary (Virolle et al., 2019a).

The incorporation of clay particles in the heterolithic point-bar deposits seems to be mostly related to hydrodynamic variations (seasonal variations in river discharge associated with seasonal TMZ position and tidal-current cycles), rather than mechanical infiltration or

bioturbation processes, as bioturbation is rarely observed and no significant variations in clay content are observed in near-surface sediments (Virolle et al., 2019a). If these postdepositional (mechanical infiltration or bioturbation) processes occurred, they are minor and do not overprint the distribution of detrital-clay grain coats in surface sediments or in the vertical facies associations of the point bar.

Diatom biofilms extensively cover the chute channel, especially during the summer (Virolle et al., 2019a). These biofilms produce abundant exopolymeric substances (EPSs), especially on the surface of the chute channel (facies F3, Virolle et al., 2019a). The role of EPSs in binding detrital clay to sand grains has been discussed in several modern estuarine studies (Shchepetkina et al., 2017, 2018; Jones, 2017; Wooldridge et al., 2017a; Virolle et al., 2019a). EPSs produced by biofilms observed in the chute channel, could be resuspended during a semidiurnal cycle (Underwood and Kromkamp, 1999) and transported in suspension, finally interacting with sand grains and clay particles on the surface of the point bar. This interaction could result in the formation of clay-coated sand grains in the zone of deposition of facies F2 (Fig. 12). Aggregates of detrital-clay grain coats in facies (F1), are observed only in depressions or hollows of detrital grains. As these grains are transported by rolling during periods of strong currents or flood events, these coats would be expected to be preserved only in depressions. It also supposes that these coats are probably inherited, preserved, and formed in another location of the point bar or facies before being incorporated in facies (F2 or F3) after sediment transport. Verhagen et al. (2020) demonstrated experimentally that clay coats can be preserved during sediment transport in turbulent flows of about 50 cm.s^{-1} . This velocity is reached during all tidal cycles in the point bar and corresponds to the formation of dunes in Facies F1. The high clay fraction ($> 30\%$ in sandy beds) in the muddy facies of core Bo-2016-W (muddy chute-channel facies) could be due to the *in situ*

production of EPS and clay entrapment by diatom biofilms (Figs 6A, B, 12; Virolle et al., 2019a). The presence of the chute channel and the mud-rich F3 facies appears to be a key point required for the production of biofilms and on the coated grains in the point bars. The chute channel traps both mud and clay (a favorable location for biofilm development), and thus appears to play an important role in binding clay to sand grains in the point bar.

Clay-Coat Composition and Mineralogy in a Modern Point Bar

The detrital-clay grain coats observed in cores are consistent with those reported in surface sediments, in the intertidal zone of the heterolithic point bar (Virolle et al., 2019a). Infrared measurements (at a very tight sampling step) provide rapid and continuous information about the clay content of the core (Fig. 8). Overall, they confirm the relative stability of clay mineralogy with depth. A focus on certain adsorption bands, such as the water band (at about 1900 nm) or the bands characteristic of aluminous phases (at 2200 and 2253 nm) reveals local accumulations of smectite or mica (Fig. 8). Locally, in core Bo-2016-W, each band exhibits a slightly increasing trend coupled with stronger fluctuations with depth (between 4 and 6 m deep) (Fig. 8). Since the clay content does not particularly increase downward, this could be due to the overall increase in the mica content. Petrographically, similar textures are observed (ridged, aggregated, or bridged textures) at all core depths. XRD analyses confirm a homogeneous clay-mineral composition in the tidal bar: (1) illite represents on average 9 wt.% of the total sediment and 45% of the clay content; (2) smectite represents on average 7 wt.% of the total sediment and 34% of the clay content; (3) chlorite represents on average 1.8 wt.% of the total sediment and 9% of the clay content; and (4) kaolinite represents on average 2.4 wt.% of the total sediment and 12% of clay content. Occasional silt-size quartz, carbonates, and pyrite are also observed embedded in detrital-

clay grain coats (Fig. 3G). The clay assemblage and the associated minerals are comparable to those reported from the Plassac tidal bar, which is located 30 km downstream in the Gironde inner estuary funnel (Virolle et al., 2019a, 2020). In contrast, the clay-mineral assemblage differs from the Richard tidal bar, which is located 70 km downstream in the Gironde outer estuary funnel. The Richard tidal-bar sediments contain less smectite (3 wt.%) and more illite (16 wt.%) (Virolle et al., 2019a, 2020).

In the alluvial plain of the Ravenglass estuary, the average clay content of 15% is slightly lower (Griffiths et al., 2019) than the 20% clay content found in the Bordeaux north point bar (20%). The majority of sand grain surfaces of the Ravenglass estuarine channels are covered by clay coats, with coat coverage greater than 30% (Griffiths et al., 2018, 2019a). The main difference in the clay-mineral assemblage is the absence of smectite (Griffiths et al., 2018, 2019a), with illite being the main clay mineral in 1–6 wt.% of the samples and representing 60% of the clay content. As in the Bordeaux North point bar, only minor amounts of kaolinite and illite (0.01–3%) were found, confirming that the Garonne estuarine channel is more turbid than the Ravenglass estuary (Griffiths et al., 2019).

Reservoir Implications

Authigenic chlorite coats have been recognized to play a significant role in preserving porosity in sandstones around the world (Pittman and Lumsden, 1968; Thomson, 1979; Ehrenberg, 1993; Bloch et al., 2002; Anjos et al., 2003; Taylor et al., 2010; Ajdukiewicz and Larese, 2012; Sun et al., 2014; Huggett et al., 2015; Saiag et al., 2016; Virolle et al., 2019b; Worden et al., 2020). Sandstones where at least 60-80% of the grains were coated (Virolle et al., 2019b; Worden et al., 2020) and/or at least 80% of quartz surfaces are covered by clay coats (Lander and Walderhaug, 1999; Taylor et al., 2010; Stricker et al., 2016) have been

found to have the best reservoir quality. Numerical models for quartz cementation suggest that complete grain coats are needed to preserve porosity in deep, high-temperature (> 70-80 deg C) reservoirs (Bloch et al., 2002; Lander et al., 2008). Modern studies have found that from 2 to 10% chlorite is needed to fully coat quartz grains (Virolle et al., 2019b; Worden et al., 2020). At all scales, in the Garonne Bordeaux North heterolithic point bar, the facies with the least mud baffles were found to be the sand-dominated facies (F1 and F2) (Figs. 3, 4, 6; Table 2). On average, in these two facies, medium-grained sandstone (mean grain size of 292 μm) were typically composed of 30% clay-coated grains, with about 5-15% of the quartz grain surfaces covered in clay, a chlorite clay content of about 2%, and a total clay fraction of 20 wt.% (Tables 1, 2, Figs. 4, 12). The clay fraction of Facies F3 was typically higher (25%) and contained a higher amount of coated grains (32%) (Table 2, Fig. 8). Those values are significantly lower than the 60-80% values and 80% quartz surface coverage proposed in the literature for chloritized reservoirs (Lander and Walderhaug, 1999; Taylor et al., 2010; Stricker et al., 2016; Virolle et al., 2019b; Worden et al., 2020). This difference is mainly due to the diagenetic process of recrystallization from detrital-clay coats to authigenic chlorite. It has been proposed that authigenic grain-coating chlorite, especially Fe-rich chlorite, does not form directly from solution by precipitation during eogenesis (Beaufort et al., 2015) but through a complex chloritization processes that involves the formation of an Fe-rich clay-mineral precursor, such as berthierine (Hornibrook and Longstaffe, 1996; Beaufort et al., 2015; Virolle et al., 2019b; Worden et al., 2020). During the chloritization process, the detrital-clay coatings initially covering 30% of the sand grains and 5-15% of the quartz grain surfaces are homogeneously redistributed around grains. After chloritization, it is likely that the percentage of coated grains in the sediment increases from 30% initially to more than 80%. It is also likely that the coat coverage (coat surface) around the detrital quartz grains

increases from an initial 5-15% to > 80%, almost complete coat coverage. From a diagenetic perspective, the detrital-clay grain coats composed of kaolinite, illite, smectite, and chlorite found in the Bordeaux North heterolithic point bar might evolve into chlorite coatings during eogenesis and burial diagenesis, and the initiation of chloritization actually begins with the formation of an early clay-mineral precursors, such as berthierine (Gould et al., 2010; Beaufort et al., 2015; Worden et al., 2020) that eventually with increasing temperature and pressure evolve into chlorite grain coats that inhibit the development of quartz cement and thus preserve deep-reservoir quality. Facies F1 and F2 have the best reservoir potential if deeply buried (more 2.5 km). We consider that the initial coated-grain content (about 30%) and initial clay-fraction content of the sediment (on average lower than 20 wt.%) could be conducive to the preservation of a porosity network (Fig. 12). In the interbedded sands of facies F3, 20-35% of clays could potentially stop development of quartz overgrowths and minimize porosity loss during burial diagenesis. However, it is likely that higher clay contents favor the development of pore-filling clay, rather than fine clay coatings, thus resulting in the loss of porosity during burial. Lastly, this study found that the mud-rich facies F3 and the chute channel facies are favorable to the development of biofilms and may play an important role in the binding of clay to sand grains in the heterolithic point bar.

Comparisons between modern analogues (such as the Garonne estuarine heterolithic point bars) and deeply buried reservoirs are key to improving predications of reservoir quality in deeply buried estuarine heterolithic point-bar reservoirs (Martinius et al., 2005) by providing critical information on the initial conditions necessary for the crystallization of chlorites during burial (Byrne et al., 2011; Shchepetkina et al., 2016b, 2018; Wooldridge et al., 2017b, 2019a; Dowey et al., 2017; Griffiths et al., 2019b, 2019a; Virolle et al., 2019a, 2020; Worden et al., 2020). The next step will be to fully understand the conditions of incipient

chloritization in shallow buried sediments (temperature, depth, pressure, chemical conditions), especially the role of iron reduction in promoting the development of chlorite precursors (such as berthierine)

CONCLUSION

(1) ^{14}C dating suggests that the Bordeaux North point bar has settled over the last 300 years. ^{137}Cs and ^{210}Pb chronologies highlight that the sedimentation rate in the chute channel is about 2 cm.y^{-1} . ^{14}C ages suggesting that the average vertical sedimentation rate ranged from 1.5 to 3.6 cm.y^{-1} in the point bar. Radiometric ages (^{14}C , ^{137}Cs , and ^{210}Pb), coupled with historical data found that the point bar has migrated laterally, approximately 200 m to the northeast since 1820, suggesting a lateral migration rate of 1 m.y^{-1} .

(2) The Garonne point bar is composed of three main facies: (1) sandy gravels; (2) heterolithic, medium-grained sand dunes; and (3) heterolithic, fine-grained sand beds and mud drapes. Sands are classified as lithic arkoses to feldspathic litharenites. The coated-grain content, coat coverage, or the mineralogy of the coats and distribution is not controlled by facies.

(3) Clay coats were observed in the entire vertical sequence of a heterolithic point bars in the modern Gironde estuarine channel (at depths down to almost 7 m). The clay assemblage is composed on average of (1) 9% illite, (2) 7% smectite, (3) 2% chlorite, and (4) 2% kaolinite. Detrital-clay grain coats, generally less than 1 mm thick (10 to several hundred μm), were observed on fine- to medium-grained sands (average grain size *ca.* $223\text{ }\mu\text{m}$). In the chute channel facies, EPSs produced by diatoms were identified that may interact directly with detrital grains. In the suspended particulate

matter of the tidal channel, EPSs could play a key role in binding clay particles around sand grains during the saltation or rolling of sand grains.

(4) On average, 31% of detrital sand grains are coated, covering 5 to 15% of the total grain surface area. These early coatings could initiate chloritization during burial diagenesis, by transforming into clay precursors (such as berthierine), thus promoting the preservation of reservoir quality by inhibiting quartz overgrowths.

ACKNOWLEDGMENTS

This work is the result of collaborative project No P04980 CLAYCOAT “CLAY COATING in shallow marine clastic deposits to improve reservoir quality prediction” between Paris-Saclay University, Bordeaux INP, Bordeaux Montaigne University, University of Poitiers, and Neptune Energy. This study has benefitted greatly from Engie and Neptune Energy funding. The authors would also like to thank Julius Nouet (Paris-Saclay University) and Thibault Duteil (Bordeaux INP) for assistance with SEM observations. We thank Anne-Sophie Canivet and Marie-Charlotte Geffray for their help with the granulometry analyses and Nicolas Saspitury (Bordeaux INP) for his help with coring of Bordeaux North point bar. We are grateful to Léa Pigot (Bordeaux INP) and Valérie Godard (Paris-Saclay University) for the high-quality thin sections. We also thank the “Sediment Archive Analysis” Platform at the EPOC laboratory (Bordeaux, France) with Isabelle Billy, Pascal Lebleu, and Olivier Ther. Marc Massault from GEOPS (Paris-Saclay University) is to be thanked for their assistance with graphite preparation and with ^{14}C counting at Gif-sur-Yvette using the energy accelerator mass spectrometer (AMS) “ECHO MICADAS - Environnement Climat et Homme Micro Carbon Dating System” of Paris-Saclay University. Two anonymous reviewers, Associate Editor

Marcia Whitlock French, and Editor Kathleen M. Marsaglia are thanked for their useful and constructive comments that improved an earlier version of this manuscript.

FIGURES

Figure 1: A) Simplified facies map of the Gironde estuary. B) Bathymetric map showing the location of the Bordeaux North point bar. C) Google Earth aerial view of the point bar. Yellow stars indicate the location of the cores sampled in this study: Bo-2016-W, Latitude (°N): 44.895911, Longitude (°E): -0.540475; Bo-2017-C, Latitude (°N): 44.896000, Longitude (°E): -0.539836; Bo-2016-E, Latitude (°N): 44.896086, Longitude (°E): -0.539217. The Bordeaux dock core was described in Jouanneau et al. (1999).

Figure 2: Left: Stratigraphic column showing principal facies of the Bordeaux North heterolithic point bar. Middle: Field photographs showing facies in the intertidal zone of the point bar. Right: Representative core photographs from the three main facies (F1, F2 and F3).

Figure 3: A) quartz-feldspar-lithic (QFL) ternary diagram (after Folk, (1974) showing the framework composition of Bordeaux North point-bar samples. B) Thin-section photomicrograph of mud drape and sand bed (BORNW-P4, 127 cm, F3). C) Thin-section photomicrograph showing clay-coatings bridges (br.), aggregates (agg.), and clay drapes (dr.) [arrows] around detrital framework grains (BORNW-P17, 590 cm, F3). D) Thin-section photomicrograph of clay-coated detrital grains showing clay-coatings bridges (br.), aggregates (agg.), and clay drapes (dr.) [arrows] (BORNW-P17, 590 cm, F3). E) Thin-section photomicrograph showing clay-coated framework grains in sand dunes, showing clay-coatings bridges (br.), aggregates (agg.), and clay drapes (dr.) [arrows] (BORN2C-P3, 84 cm,

F2). F) SEM image showing clay coatings on a quartz grain from sandy gravel facies [yellow box indicates location of G] (BORNE-P14, 438 cm, F1 facies). G) Close-up view of the clay coat displayed in Part F. The clay coatings are mainly composed of detrital clay minerals and occasional silt-size grains and authigenic pyrite [+ marks location of EDS spot analysis]. H) EDS spectrum of a clay coat on detrital quartz seen in Part G, Spots 1 consists primarily of detrital clay; KEY: Qz = quartz; Li = lithoclast; Fd = feldspar; W = wood debris. See Figure 4 for the location of the thin sections.

Figure 4: E-W stratigraphic cross section across the Bordeaux North point bar showing the three cores analyzed in this study: Bo-2016-W; Bo-2017-C and Bo-2016-E with associated ages. pMC: percent modern carbon (modern age).

Figure 5: A) Vertical profiles showing ^{137}Cs and ^{210}Pb activities along core Bo-2016-W. This part of the core corresponds to facies F3 of the chute channel (see Fig. 4). B) Core photograph of facies F3 and ages obtained after data processing. C) Time (horizontal-axis) vs. depth (vertical-axis) plot constructed using ^{137}Cs and ^{210}Pb activities.

Figure 6: A) Thin-section microphotographs showing diatoms embedded in detrital-clay grain coats in facies F3 from the Bordeaux North point bar (BORNW-P5, 179 cm). B) SEM image showing diatom embedded in detrital-clay grain coats in facies F2 from the Bordeaux North point bar (BORN2C-P3, 84 cm). C, D, E) Cryo-SEM images of sediment sample from the Bordeaux North point bar (depth 25 cm). C) Low-magnification SEM view of quartz sand grain coated with an EPS-clay complex. D) Composite EDS spectra of the two analyzed spots marked with + in Part E. Spot 1 [black line] confirms detrital quartz grain host. Spot 2 appears to be an aluminous phyllosilicate (clay-mineral signature). E) SEM close-up view of Part C showing the alveolar network formed by EPS intermixed with patchy clay platelets. See Figure 4 for the location of samples BORNW-P5 and BORN2C-P3.

Figure 7: Histograms showing average grain-coat content per facies divided into coat coverage classes. The sum of the coat coverage classes gives the total coated-grain content for each facies.

Figure 8: Summary core logs showing evolution with depth of mean grain size, percentage of < 2 μm particles, and relative fraction of clay minerals, coated-grain content, and FTIR measurements for the three cores from the Bordeaux North point bar.

Figure 9: Plots representing the mean proportions in % of A) coated-grain content (from image analysis), B) clay-fraction content (weighted percentage of clay fraction from total volume), C) smectite (from XRD analysis), D) illite (from XRD analysis), E) kaolinite (from XRD analysis), and F) chlorite (from XRD analysis) in each facies. Above each histogram is the number of samples analyzed.

Figure 10: X-Ray diffractograms of the < 2 μm fraction showing dominant clay minerals (BORNW-11, depth: 281 cm). See Fig. 4 for the location of this sample.

Figure 11: Aerial photographs showing lateral bank accretion from 1820–1866 to present of the Bordeaux North point bar (Source: IGN maps, <https://remonterletemps.ign.fr>).

Figure 12: A) Synthetic diagram of the heterolithic point-bar deposits at macro- (core) and micro- (thin-section) scales. The core drawing illustrates the heterolithic vertical facies association, while the thin-section documents how the clay coats are distributed. B) Cartoon summarizing how detrital-clay coatings may form on a heterolithic point bar. C) Table showing the average clay values, total clay, and grain-coat coverage by facies. KEY: EPS: exopolymeric substances.

REFERENCES

- 692 Aagaard, P., Jahren, J.S., Harstad, A.O., Nilsen, O., and Ramm, M., 2000, Formation of grain-
693 coating chlorite in sandstones. Laboratory synthesized vs. natural occurrences: *Clay*
694 *Minerals*, v. 35, p. 261–269, doi:10.1180/000985500546639.
- 695 Ajdukiewicz, J.M., and Larese, R.E., 2012, How clay grain coats inhibit quartz cement and
696 preserve porosity in deeply buried sandstones: Observations and experiments:
697 *American Association of Petroleum Geologists, Bulletin*, v. 96, p. 2091–2119,
698 doi:10.1306/02211211075.
- 699 Allen, G.P., 1991, Sedimentary processes and facies in the Gironde estuary: a recent model
700 for macrotidal estuarine systems, *in* Smith, D.G., Zaitlin, B.A., Reinson, G.E., and
701 Rahmani, R.A. eds., *Clastic Tidal Sedimentology, Recognition Criteria and Facies*
702 *Models*, v. Memoir 16, p. 29–39.
- 703 Allen, G.P., and Posamentier, H.W., 1993, Sequence Stratigraphy and Facies Model of an
704 Incised Valley Fill: The Gironde Estuary, France: *Journal of Sedimentary Petrology*,
705 v. 63, doi:10.1306/D4267B09-2B26-11D7-8648000102C1865D.
- 706 Anjos, S.M.C., De Ros, L.F., and Silva, C.M.A., 2003, Chlorite Authigenesis and Porosity
707 Preservation in the Upper Cretaceous Marine Sandstones of the Santos Basin,
708 Offshore Eastern Brazil, *in* Worden, R.H. and Morad, S. eds., *Clay Mineral Cements*
709 *in Sandstones*, Oxford, UK, Blackwell Publishing Ltd., p. 289–316,
710 doi:10.1002/9781444304336.ch13.
- 711 Appleby, P.G., Nolan, P.J., Gifford, D.W., Godfrey, M.J., Oldfield, F., Anderson, N.J., and
712 Battarbee, R.W., 1986, ^{210}Pb dating by low background gamma counting:
713 *Hydrobiologia*, v. 143, p. 21–27, doi:10.1007/BF00026640.
- 714 Appleby, P.G., Richardson, N., and Nolan, P.J., 1992, Self-absorption corrections for well-
715 type germanium detectors: *Nuclear Instruments and Methods in Physics Research*
716 *Section B: Beam Interactions with Materials and Atoms*, v. 71, p. 228–233,
717 doi:10.1016/0168-583X(92)95328-O.
- 718 Beaufort, D., Rigault, C., Billon, S., Billault, V., Inoue, A., Inoue, S., and Patrier, P., 2015,
719 Chlorite and chloritization processes through mixed-layer mineral series in low-
720 temperature geological systems – a review: *Clay Minerals*, v. 50, p. 497–523,
721 doi:10.1180/claymin.2015.050.4.06.
- 722 Billy, J., Chaumillon, E., Féliès, H., and Poirier, C., 2012, Tidal and fluvial controls on the
723 morphological evolution of a lobate estuarine tidal bar: The Plassac Tidal Bar in the
724 Gironde Estuary (France): *Geomorphology*, v. 169–170, p. 86–97,
725 doi:10.1016/j.geomorph.2012.04.015.
- 726 Bloch, S., Lander, R.H., and Bonnell, L., 2002, Anomalously high porosity and permeability
727 in deeply buried sandstone reservoirs: Origin and predictability: *American Association*
728 *of Petroleum Geologists, Bulletin*, v. 86, p. 301–328.
- 729 Blong, R.J., and Gillespie, R., 1978, Fluvially transported charcoal gives erroneous ^{14}C ages
730 for recent deposits: *Nature*, v. 271, p. 739–741.
- 731 Boersma, J.R., and Terwindt, J.H.J., 1981, Neap–spring tide sequences of intertidal shoal
732 deposits in a mesotidal estuary: *Sedimentology*, v. 28, p. 151–170.

733 Braissant, O., Decho, A.W., Dupraz, C., Glunk, C., Przekop, K.M., and Visscher, P.T., 2007,
734 Exopolymeric substances of sulfate-reducing bacteria: Interactions with calcium at
735 alkaline pH and implication for formation of carbonate minerals: *Geobiology*, v. 5, p.
736 401–411, doi:10.1111/j.1472-4669.2007.00117.x.

737 Byrne, G.M., Worden, R.H., Hodgson, D.M., Polya, D.A., Lythgoe, P.R., Barrie, C.D., and
738 Boyce, A.J., 2011, Understanding the fate of iron in a modern temperate estuary:
739 Leirárvogur, Iceland: *Applied Geochemistry*, v. 26, p. S16–S19,
740 doi:10.1016/j.apgeochem.2011.03.018.

741 Castaing, P., and Allen, G.P., 1981, Mechanisms controlling seaward escape of suspended
742 sediment from the Gironde: A macrotidal estuary in France: *Marine Geology*, v. 40, p.
743 101–118, doi:10.1016/0025-3227(81)90045-1.

744 Chaumillon, E., Féliès, H., Billy, J., Breilh, J.-F., and Richetti, H., 2013, Tidal and fluvial
745 controls on the internal architecture and sedimentary facies of a lobate estuarine tidal
746 bar (The Plassac Tidal Bar in the Gironde Estuary, France): *Marine Geology*, v. 346,
747 p. 58–72, doi:10.1016/j.margeo.2013.07.017.

748 Cosma, M., Ghinassi, M., D'Alpaos, A., Roner, M., Finotello, A., Tommasini, L., and Gatto,
749 R., 2019, Point-bar brink and channel thalweg trajectories depicting interaction
750 between vertical and lateral shifts of microtidal channels in the Venice Lagoon (Italy):
751 *Geomorphology*, v. 342, p. 37–50, doi:10.1016/j.geomorph.2019.06.009.

752 Coynel, A., Schafer, J., Hurtrez, J., Dumas, J., Etcheber, H., and Blanc, G., 2004, Sampling
753 frequency and accuracy of SPM flux estimates in two contrasted drainage basins:
754 *Science of The Total Environment*, v. 330, p. 233–247,
755 doi:10.1016/j.scitotenv.2004.04.003.

756 D'Alpaos, A., Ghinassi, M., Finotello, A., Brivio, L., Bellucci, L.G., and Marani, M., 2017,
757 Tidal meander migration and dynamics: A case study from the Venice Lagoon:
758 *Marine and Petroleum Geology*, v. 87, p. 80–90,
759 doi:10.1016/j.marpetgeo.2017.04.012.

760 De Mowbray, T., and Visser, M.J., 1984, Reactivation surfaces in subtidal channel deposits,
761 Oosterschelde, Southwest Netherlands: *Journal of Sedimentary Petrology*, v. 54, p.
762 811–824.

763 De Resseguier, A., 1983, A portable coring device for use in the intertidal environment:
764 *Marine Geology*, v. 52, p. M19–M23, doi:10.1016/0025-3227(83)90015-4.

765 Decho, A.W., 2000, Microbial biofilms in intertidal systems: an overview: *Continental Shelf*
766 *Research*, v. 20, p. 1257–1273, doi:10.1016/S0278-4343(00)00022-4.

767 Donnici, S., Madricardo, F., and Serandrei-Barbero, R., 2017, Sedimentation rate and lateral
768 migration of tidal channels in the Lagoon of Venice (Northern Italy): *Estuarine,*
769 *Coastal and Shelf Science*, v. 198, p. 354–366, doi:10.1016/j.ecss.2017.02.016.

770 Dowey, P.J., Worden, R.H., Utley, J., and Hodgson, D.M., 2017, Sedimentary controls on
771 modern sand grain coat formation: *Sedimentary Geology*, v. 353, p. 46–63,
772 doi:10.1016/j.sedgeo.2017.03.001.

- 773 Duteil, T., Bourillot, R., Grégoire, B., Virolle, M., Brigaud, B., Nouet, J., Braissant, O.,
774 Portier, E., Fénies, H., Patrier, P., Gontier, E., Svahn, I., and Visscher, P.T., 2020,
775 Experimental formation of clay-coated sand grains using diatom biofilm exopolymers:
776 *Geology*, v. 48, p. 1012–1017, doi:10.1130/G47418.1.
- 777 Ehrenberg, S.N., 1993, Preservation of anomalously high porosity in deeply buried sandstones
778 by grain-coating chlorite: examples from the Norwegian continental shelf: *American*
779 *Association of Petroleum Geologists, Bulletin*, v. 77, p. 1260–1286.
- 780 Ely, L.L., Webb, R.H., and Enzel, Y., 1992, Accuracy of post-bomb ^{137}Cs and ^{14}C in dating
781 fluvial deposits: *Quaternary Research*, v. 38, p. 196–204, doi:10.1016/0033-
782 5894(92)90056-O.
- 783 Etcheber, H., Schmidt, S., Sottolichio, A., Maneux, E., Chabaux, G., Escalier, J.-M.,
784 Wennekes, H., Derriennic, H., Schmeltz, M., Quémener, L., Repecaud, M., Woerther,
785 P., and Castaing, P., 2011, Monitoring water quality in estuarine environments:
786 lessons from the MAGEST monitoring program in the Gironde fluvial-estuarine
787 system: *Hydrology and Earth System Sciences*, v. 15, p. 831–840, doi:10.5194/hess-
788 15-831-2011.
- 789 Evrard, O., Chaboche, P.-A., Ramon, R., Foucher, A., and Laceby, J.P., 2020, A global
790 review of sediment source fingerprinting research incorporating fallout radiocesium
791 (^{137}Cs): *Geomorphology*, v. 362, p. 107103, doi:10.1016/j.geomorph.2020.107103.
- 792 Fénies, H., Resseguier, A.D., and Tastet, J., 1999, Intertidal clay-drape couplets (Gironde
793 estuary, France): *Sedimentology*, v. 46, p. 1–15, doi:10.1046/j.1365-
794 3091.1999.00196.x.
- 795 Fénies, H., and Tastet, J.-P., 1998, Facies and architecture of an estuarine tidal bar (the
796 Trompeloup bar, Gironde Estuary, SW France): *Marine Geology*, v. 150, p. 149–169,
797 doi:10.1016/S0025-3227(98)00059-0.
- 798 Finotello, A., Lanzoni, S., Ghinassi, M., Marani, M., Rinaldo, A., and D’Alpaos, A., 2018,
799 Field migration rates of tidal meanders recapitulate fluvial morphodynamics:
800 *Proceedings of the National Academy of Sciences*, v. 115, p. 1463–1468,
801 doi:10.1073/pnas.1711330115.
- 802 Folk, R.L., 1974, *Petrology of Sedimentary Rocks*: Austin, Texas, Hemphill Publishing
803 Company, v. 182, 184 p.
- 804 Ghinassi, M., D’alpaos, A., Gasparotto, A., Carniello, L., Brivio, L., Finotello, A., Roner, M.,
805 Franceschinis, E., Realdon, N., Howes, N., and Cantelli, A., 2018, Morphodynamic
806 evolution and stratal architecture of translating tidal point bars: Inferences from the
807 northern Venice Lagoon (Italy) (J. Howell, Ed.): *Sedimentology*, v. 65, p. 1354–1377,
808 doi:10.1111/sed.12425.
- 809 Gould, K., Pe-Piper, G., and Piper, D.J.W., 2010, Relationship of diagenetic chlorite rims to
810 depositional facies in Lower Cretaceous reservoir sandstones of the Scotian Basin:
811 *Sedimentology*, v. 57, p. 587–610, doi:10.1111/j.1365-3091.2009.01106.x.
- 812 Griffiths, J., Worden, R.H., Wooldridge, L.J., Utley, J.E.P., and Duller, R.A., 2019a,
813 Compositional variation in modern estuarine sands: Predicting major controls on

814 sandstone reservoir quality: American Association of Petroleum Geologists, Bulletin,
815 v. 103, p. 797–833, doi:10.1306/09181818025.

816 Griffiths, J., Worden, R.H., Wooldridge, L.J., Utley, J.E.P., and Duller, R.A., 2018, Detrital
817 Clay Coats, Clay Minerals, and Pyrite: A Modern Shallow-Core Analogue For
818 Ancient and Deeply Buried Estuarine Sandstones: Journal of Sedimentary Research, v.
819 88, p. 1205–1237, doi:10.2110/jsr.2018.56.

820 Griffiths, J., Worden, R.H., Wooldridge, L.J., Utley, J.E.P., Duller, R.A., and Edge, R.L.,
821 2019b, Estuarine clay mineral distribution: Modern analogue for ancient sandstone
822 reservoir quality prediction: Sedimentology, v. 66, p. 2011–2047,
823 doi:10.1111/sed.12571.

824 Grim, R.E., 1942, Modern Concepts of Clay Materials: The Journal of Geology, v. 50, p.
825 225–275, doi:10.1086/625050.

826 Grousset, F.E., Jouanneau, J.M., Castaing, P., Lavaux, G., and Latouche, C., 1999, A 70 year
827 Record of Contamination from Industrial Activity Along the Garonne River and its
828 Tributaries (SW France): Estuarine, Coastal and Shelf Science, v. 48, p. 401–414,
829 doi:10.1006/ecss.1998.0435.

830 Haile, B.G., Hellevang, H., Aagaard, P., and Jahren, J., 2015, Experimental nucleation and
831 growth of smectite and chlorite coatings on clean feldspar and quartz grain surfaces:
832 Marine and Petroleum Geology, v. 68, p. 664–674,
833 doi:10.1016/j.marpetgeo.2015.02.006.

834 Hornibrook, E.R.C., and Longstaffe, F.J., 1996, Berthierine from the Lower Cretaceous
835 Clearwater Formation, Alberta, Canada: Clays and Clay Minerals, v. 44, p. 1–21,
836 doi:10.1346/CCMN.1996.0440101.

837 Huggett, J.M., Burley, S.D., Longstaffe, F.J., Saha, S., and Oates, M.J., 2015, The nature and
838 origin of authigenic chlorite and related cements in Oligo-Miocene reservoir
839 Sandstones, Tapti Gas Fields, Surat Depression, Offshore Western India: Journal of
840 Petroleum Geology, v. 38, p. 383–409, doi:10.1111/jpg.12618.

841 Jalón-Rojas, I., Schmidt, S., and Sottolichio, A., 2015, Turbidity in the fluvial Gironde
842 Estuary (southwest France) based on 10-year continuous monitoring: sensitivity to
843 hydrological conditions: Hydrology and Earth System Sciences, v. 19, p. 2805–2819,
844 doi:10.5194/hess-19-2805-2015.

845 Jones, S., 2017, Goo, glue, and grain binding: Importance of biofilms for diagenesis in
846 sandstones: Geology, v. 45, p. 959–960, doi:10.1130/focus102017.1.

847 Jordan, D.W., and Pryor, W.A., 1992, Hierarchical Levels of Heterogeneity in a Mississippi
848 River Meander Belt and Application to Reservoir Systems: Geologic Note (1):
849 American Association of Petroleum Geologists, Bulletin, v. 76,
850 doi:10.1306/BDF8A6A-1718-11D7-8645000102C1865D.

851 Jouanneau, J.-M., Castaing, P., Grousset, F., Buat-Ménard, P., and Pedemay, P., 1999,
852 Enregistrement sédimentaire et chronologie (¹³⁷Cs) d'une contamination en cadmium
853 dans l'estuaire de la Gironde (France): Comptes Rendus de l'Académie des Sciences -
854 Series IIA - Earth and Planetary Science, v. 329, p. 265–270, doi:10.1016/S1251-

- 8050(99)80245-6.
- Kochel, R.C., and Baker, V., 1988, Paleoflood analysis using slackwater deposits, *in* Baker, V., Kochel, R.C., and Patton, P.C. eds., *Flood Geomorphology*, Wiley-Interscience, p. 357–376.
- La Croix, A.D., Dashtgard, S.E., Gingras, M.K., Hauck, T.E., and MacEachern, J.A., 2015, Bioturbation trends across the freshwater to brackish-water transition in rivers: Palaeogeography, Palaeoclimatology, Palaeoecology, v. 440, p. 66–77, doi:10.1016/j.palaeo.2015.08.030.
- La Croix, A.D., Dashtgard, S.E., and MacEachern, J.A., 2019, Using a modern analogue to interpret depositional position in ancient fluvial-tidal channels: Example from the McMurray Formation, Canada: *Geoscience Frontiers*, v. 10, p. 2219–2238, doi:10.1016/j.gsf.2019.03.008.
- Lander, R.H., Larese, R.E., and Bonnell, L.M., 2008, Toward more accurate quartz cement models: The importance of euhedral versus noneuhedral growth rates: *American Association of Petroleum Geologists, Bulletin*, v. 92, p. 1537–1563, doi:10.1306/07160808037.
- Lander, R.H., and Walderhaug, O., 1999, Predicting Porosity through Simulating Sandstone Compaction and Quartz Cementation: *American Association of Petroleum Geologists, Bulletin*, v. 83, p. 433–449, doi:10.1306/00AA9BC4-1730-11D7-8645000102C1865D.
- Latouche, C., 1971, Les argiles des bassins alluvionnaires aquitains et des dépendances océaniques: contribution à l'étude d'un environnement [Thèse de doctorat, Université de Bordeaux]: Institut de Geologie du Bassin d'Aquitaine, 415 p.
- Long, A., and Rippeteau, B., 1974, Testing Contemporaneity and Averaging Radiocarbon Dates: *American Antiquity*, v. 39, p. 205–215, doi:10.2307/279583.
- Malarkey, J., Baas, J.H., Hope, J.A., Aspden, R.J., Parsons, D.R., Peakall, J., Paterson, D.M., Schindler, R.J., Ye, L., Lichtman, I.D., Bass, S.J., Davies, A.G., Manning, A.J., and Thorne, P.D., 2015, The pervasive role of biological cohesion in bedform development: *Nature Communications*, v. 6, p. 6257, doi:10.1038/ncomms7257.
- Martinius, A.W., Ringrose, P.S., Brostrøm, C., Elfenbein, C., Næss, A., and Ringås, J.E., 2005, Reservoir challenges of heterolithic tidal sandstone reservoirs in the Halten Terrace, mid-Norway: *Petroleum Geoscience*, v. 11, p. 3–16, doi:10.1144/1354-079304-629.
- Monna, F., Dominik, J., Loizeau, J.-Luc., Pardos, M., and Arpagaus, P., 1999, Origin and Evolution of Pb in Sediments of Lake Geneva (Switzerland–France). Establishing a Stable Pb Record: *Environmental Science & Technology*, v. 33, p. 2850–2857, doi:10.1021/es9902468.
- Musial, G., Reynaud, J.-Y., Gingras, M.K., Féliès, H., Labourdette, R., and Parize, O., 2012, Subsurface and outcrop characterization of large tidally influenced point bars of the Cretaceous McMurray Formation (Alberta, Canada): *Sedimentary Geology*, v. 279, p. 156–172, doi:10.1016/j.sedgeo.2011.04.020.

- 896 Pace, A., Bourillot, R., Bouton, A., Vennin, E., Braissant, O., Dupraz, C., Duteil, T.,
897 Bundelewa, I., Patrier, P., Galaup, S., Yokoyama, Y., Franceschi, M., Virgone, A., and
898 Visscher, P.T., 2018, Formation of stromatolite lamina at the interface of oxygenic-
899 anoxygenic photosynthesis: *Geobiology*, v. 16, p. 378–398, doi:10.1111/gbi.12281.
- 900 Parra, M., Trouky, H., Jouanneau, J.-M., Grousset, F., Latouche, C., and Castaing, P., 1998,
901 Étude isotopique (Sr-Nd) de l'origine des dépôts fins holocènes du littoral atlantique
902 (S-O France): *Oceanologica Acta*, v. 21, p. 631–644, doi:10.1016/S0399-
903 1784(99)80022-X.
- 904 Petschick, R., 2002, MacDiff 4.2.6 - Manual: 61 p., [http://www.geol-pal.uni-](http://www.geol-pal.uni-frankfurt.de/Staff/Homepages/Petschick/PDFs/MacDiff%20Manual%20E.pdf)
905 [frankfurt.de/Staff/Homepages/Petschick/PDFs/MacDiff%20Manual%20E.pdf](http://www.geol-pal.uni-frankfurt.de/Staff/Homepages/Petschick/PDFs/MacDiff%20Manual%20E.pdf).
- 906 Pittman, E.D., and Lumsden, D.N., 1968, Relationship between chlorite coatings on quartz
907 grains and porosity, Spiro Sand, Oklahoma: *Journal of Sedimentary Petrology*, v. 38,
908 p. 668–670, doi:10.1306/74D71A28-2B21-11D7-8648000102C1865D.
- 909 Pourchet, M., Pinglot, J.F., and Mélières, M.A., 1989, Cesium 137 and lead 210 in alpine lake
910 sediments: Measurements and modeling of mixing processes: *Journal of Geophysical*
911 *Research*, v. 94, p. 12761–12770, doi:10.1029/JC094iC09p12761.
- 912 Pranter, M.J., Ellison, A.I., Cole, R.D., and Patterson, P.E., 2007, Analysis and modeling of
913 intermediate-scale reservoir heterogeneity based on a fluvial point-bar outcrop analog,
914 Williams Fork Formation, Piceance Basin, Colorado: *American Association of*
915 *Petroleum Geologists, Bulletin*, v. 91, p. 1025–1051, doi:10.1306/02010706102.
- 916 Roduit, N., 2007, JMicroVision: un logiciel d'analyse d'images pétrographiques polyvalent:
917 Section de Sciences de la Terre, Université de Genève, 116 p., 10.13097/archive-
918 ouverte/unige:468.
- 919 Saïag, J., Brigaud, B., Portier, É., Desaubliaux, G., Bucherie, A., Miska, S., and Pagel, M.,
920 2016, Sedimentological control on the diagenesis and reservoir quality of tidal
921 sandstones of the Upper Cape Hay Formation (Permian, Bonaparte Basin, Australia):
922 *Marine and Petroleum Geology*, v. 77, p. 597–624,
923 doi:10.1016/j.marpetgeo.2016.07.002.
- 924 Sarkar, S., Banerjee, S., Eriksson, P.G., and Catuneanu, O., 2005, Microbial mat control on
925 siliciclastic Precambrian sequence stratigraphic architecture: Examples from India:
926 *Sedimentary Geology*, v. 176, p. 195–209, doi:10.1016/j.sedgeo.2004.12.012.
- 927 Shchepetkina, A., Gingras, M.K., and Pemberton, S.G., 2018, Modern observations of
928 floccule ripples: Petitcodiac River estuary, New Brunswick, Canada: *Sedimentology*,
929 v. 65, p. 582–596, doi:10.1111/sed.12393.
- 930 Shchepetkina, A., Gingras, M.K., and Pemberton, S.G., 2016a, Sedimentology and ichnology
931 of the fluvial reach to inner estuary of the Ogeechee River estuary, Georgia, USA:
932 *Sedimentary Geology*, v. 342, p. 202–217, doi:10.1016/j.sedgeo.2016.07.005.
- 933 Shchepetkina, A., Gingras, M.K., Zonneveld, J.-P., and Pemberton, S.G., 2016b, Sedimentary
934 fabrics of the macrotidal, mud-dominated, inner estuary to fluvio-tidal transition zone,
935 Petitcodiac River estuary, New Brunswick, Canada: *Sedimentary Geology*, v. 333, p.
936 147–163, doi:10.1016/j.sedgeo.2015.12.015.

- 937 Shchepetkina, A., Gingras, M.K., Zonneveld, J.-P., and Pemberton, S.G., 2017, Silt- and
938 Bioclastic-Rich Flocs and Their Relationship to Sedimentary Structures: Modern
939 Observations from the Petitcodiac River Estuary: *Estuaries and Coasts*, v. 40, p. 947–
940 966, doi:10.1007/s12237-016-0186-x.
- 941 Smith, D.J., and Underwood, G.J.C., 1998, Exopolymer production by intertidal epipellic
942 diatoms: *Limnology and Oceanography*, v. 43, p. 1578–1591,
943 doi:10.4319/lo.1998.43.7.1578.
- 944 Sottolichio, A., Castaing, P., Etcheber, H., Maneux, E., Schmeltz, M., and Schmidt, S., 2011,
945 Observations of suspended sediment dynamics in a highly turbid macrotidal estuary,
946 derived from continuous monitoring: *Journal of Coastal Research*, v. 64, p. 1579–
947 1583.
- 948 Stoodley, P., Cargo, R., Rupp, C.J., Wilson, S., and Klapper, I., 2002, Biofilm material
949 properties as related to shear-induced deformation and detachment phenomena:
950 *Journal of Industrial Microbiology and Biotechnology*, v. 29, p. 361–367,
951 doi:10.1038/sj.jim.7000282.
- 952 Stricker, S., Jones, S.J., Sathar, S., Bowen, L., and Oxtoby, N., 2016, Exceptional reservoir
953 quality in HPHT reservoir settings: Examples from the Skagerrak Formation of the
954 Heron Cluster, North Sea, UK: *Marine and Petroleum Geology*, v. 77, p. 198–215,
955 doi:10.1016/j.marpetgeo.2016.02.003.
- 956 Sun, Z.-X., Sun, Z.-L., Yao, J., Wu, M.-L., Liu, J.-R., Dou, Z., and Pei, C., 2014, Porosity
957 preservation due to authigenic chlorite coatings in deeply buried Upper Triassic
958 Xujiahe Formation Sandstones, Sichuan Basin, Western China: *Journal of Petroleum*
959 *Geology*, v. 37, p. 251–267, doi:10.1111/jpg.12582.
- 960 Taylor, T.R., Giles, M.R., Hathon, L.A., Diggs, T.N., Braunsdorf, N.R., Birbiglia, G.V.,
961 Kittridge, M.G., Macaulay, C.I., and Espejo, I.S., 2010, Sandstone diagenesis and
962 reservoir quality prediction: Models, myths, and reality: *American Association of*
963 *Petroleum Geologists, Bulletin*, v. 94, p. 1093–1132, doi:10.1306/04211009123.
- 964 Thomson, A., 1979, Preservation of porosity in the deep Woodbine/Tuscaloosa Trend,
965 Louisiana, *in* Gulf Coast Association of Geological Societies Transactions, San
966 Antonio, Texas, 29th Annual Meeting, v. 29, p. 396–403.
- 967 Underwood, G.C., and Kromkamp, J., 1999, Primary production by phytoplankton and
968 microphytobenthos in estuaries: *Advances in ecological research*, v. 29, p. 93–153.
- 969 Verhagen, I.T.E., Crisóstomo-Figueroa, A., Utley, J.E.P., and Worden, R.H., 2020, Abrasion
970 of detrital grain-coating clays during sediment transport: Implications for diagenetic
971 clay coats: *Sedimentary Geology*, p. 105653, doi:10.1016/j.sedgeo.2020.105653.
- 972 Virolle, M., Brigaud, B., Bourillot, R., Féliès, H., Portier, E., Duteil, T., Nouet, J., Patrier, P.,
973 and Beaufort, D., 2019a, Detrital clay grain coats in estuarine clastic deposits: origin
974 and spatial distribution within a modern sedimentary system, the Gironde Estuary
975 (south-west France): *Sedimentology*, v. 66, p. 859–894, doi:10.1111/sed.12520.
- 976 Virolle, M., Brigaud, B., Luby, S., Portier, E., Féliès, H., Bourillot, R., Patrier, P., and
977 Beaufort, D., 2019b, Influence of sedimentation and detrital clay grain coats on

978 chloritized sandstone reservoir qualities: Insights from comparisons between ancient
979 tidal heterolithic sandstones and a modern estuarine system: *Marine and Petroleum*
980 *Geology*, v. 107, p. 163–184, doi:10.1016/j.marpetgeo.2019.05.010.

981 Virolle, M., Fénies, H., Brigaud, B., Bourillot, R., Portier, E., Patrier, P., Beaufort, D., Jalon-
982 Rojas, I., Derriennic, H., and Miska, S., 2020, Facies associations, detrital clay grain
983 coats and mineralogical characterization of the Gironde estuary tidal bars: A modern
984 analogue for deeply buried estuarine sandstone reservoirs: *Marine and Petroleum*
985 *Geology*, p. 104225, doi:https://doi.org/10.1016/j.marpetgeo.2020.104225.

986 Visser, M.J., 1980, Neap-spring cycles reflected in Holocene subtidal large-scale bedform
987 deposits: a preliminary note: *Geology*, v. 8, p. 543–546.

988 Webb, R.H., O'Connor, J.E., and Baker, V., 1988, Paleohydrologic reconstruction of flood
989 frequency on the Escalante River, south-central Utah, *in* Baker, V., Kochel, R.C., and
990 Patton, P.C. eds., *Flood Geomorphology*, Wiley-Interscience, p. 403–418.

991 Williams, H.F.L., and Hamilton, T.S., 1995, Sedimentary Dynamics of an Eroding Tidal
992 Marsh Derived from Stratigraphic Records of ¹³⁷Cs Fallout, Fraser Delta, British
993 Columbia, Canada: *Journal of Coastal Research*, v. 11, p. 1145–1156.

994 Wooldridge, L.J., Worden, R.H., Griffiths, J., Thompson, A., and Chung, P., 2017a, Biofilm
995 origin of clay-coated sand grains: *Geology*, v. 45, p. 875–878, doi:10.1130/G39161.1.

996 Wooldridge, L.J., Worden, R.H., Griffiths, J., and Utley, J.E.P., 2019a, Clay- coat diversity in
997 marginal marine sediments: *Sedimentology*, doi:10.1111/sed.12538.

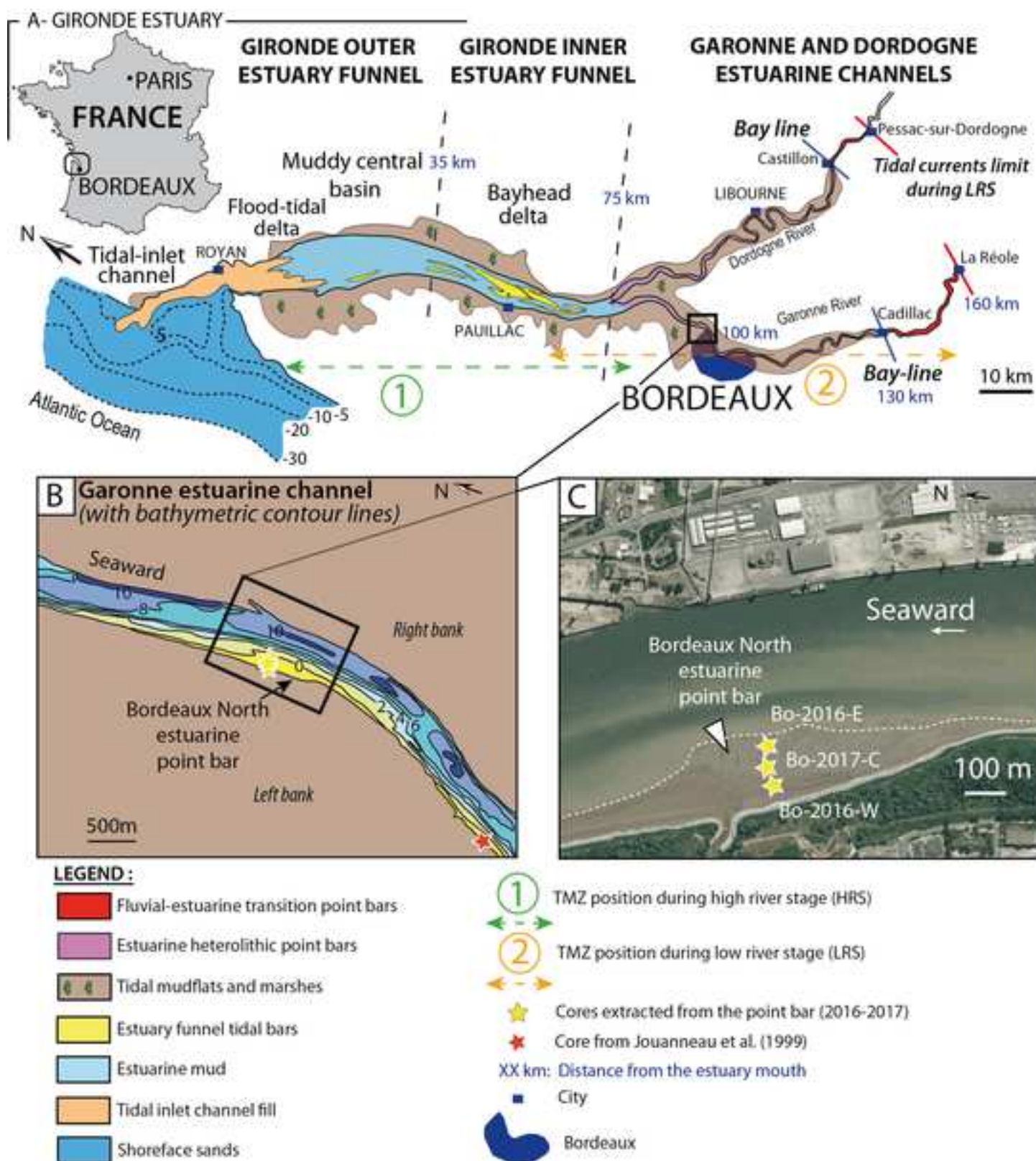
998 Wooldridge, L.J., Worden, R.H., Griffiths, J., and Utley, J.E.P., 2017b, Clay-Coated Sand
999 Grains in Petroleum Reservoirs: Understanding Their Distribution Via a Modern
1000 Analogue: *Journal of Sedimentary Research*, v. 87, p. 338–352,
1001 doi:10.2110/jsr.2017.20.

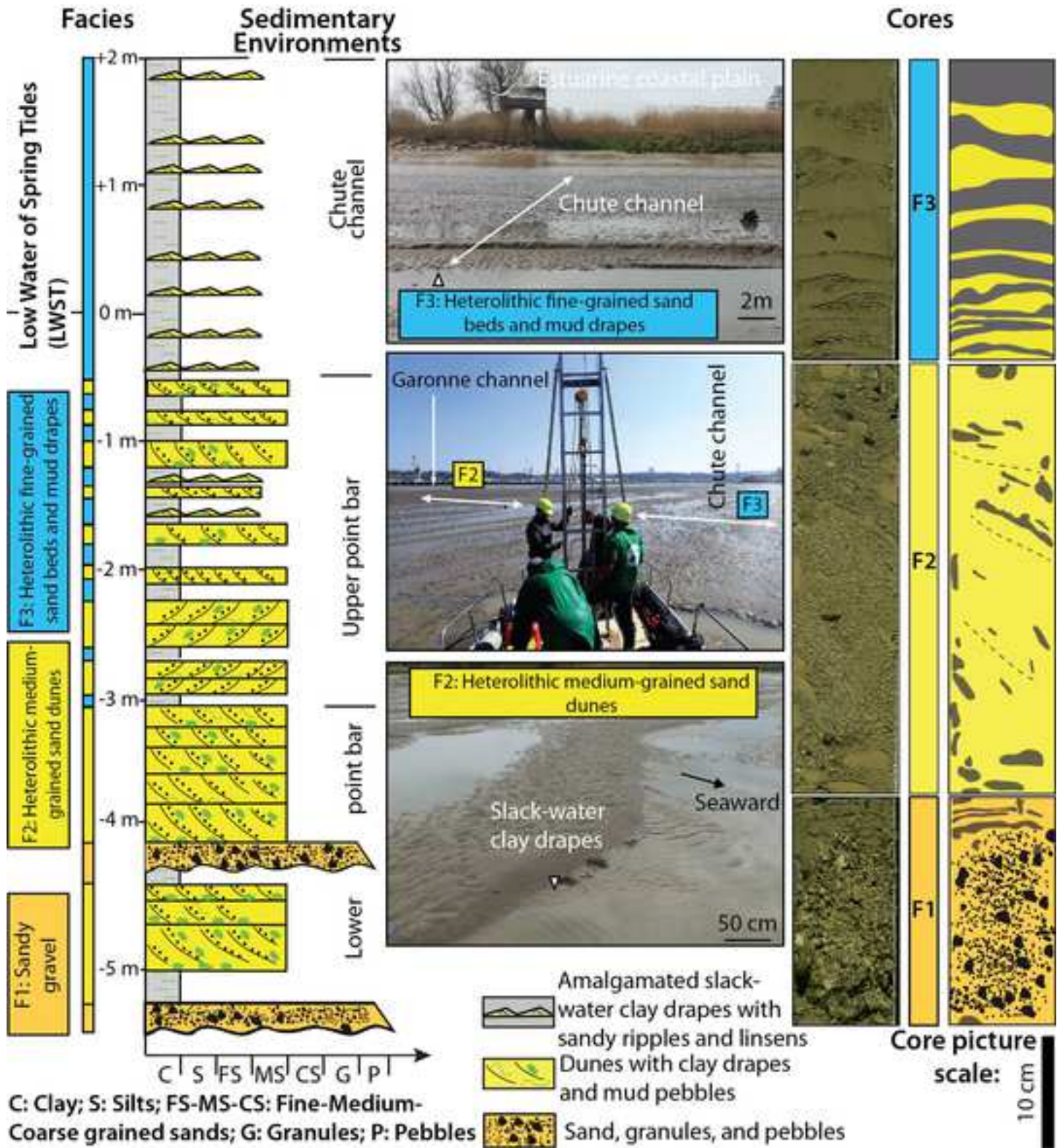
1002 Wooldridge, L.J., Worden, R.H., Griffiths, J., and Utley, J.E.P., 2019b, How to Quantify
1003 Clay-Coat Grain Coverage in Modern and Ancient Sediments: *Journal of Sedimentary*
1004 *Research*, v. 89, p. 135–146, doi:10.2110/jsr.2019.6.

1005 Worden, R.H., Griffiths, J., Wooldridge, L.J., Utley, J.E.P., Lawan, A.Y., Muhammed, D.D.,
1006 Simon, N., and Armitage, P.J., 2020, Chlorite in sandstones: *Earth-Science Reviews*,
1007 v. 204, p. 103105, doi:10.1016/j.earscirev.2020.103105.

1008 Worden, R.H., and Morad, S., 2003, Clay Minerals in Sandstones: Controls on Formation,
1009 Distribution and Evolution, *in* Worden, R.H. and Morad, S. eds., *Clay Mineral*
1010 *Cements in Sandstones*, Oxford, UK, Blackwell Publishing Ltd., p. 3–41,
1011 doi:10.1002/9781444304336.ch1.

1012





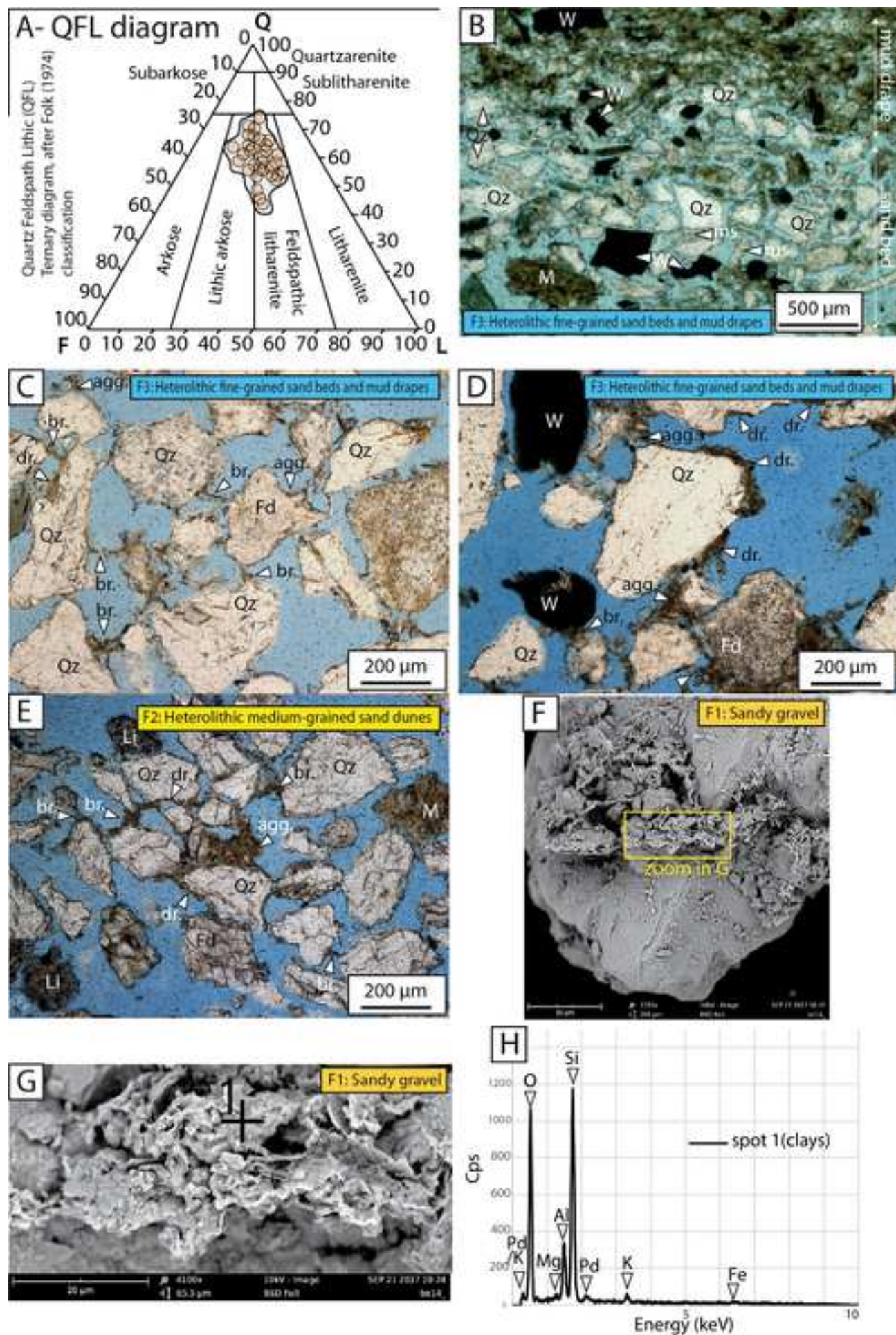


Figure 4

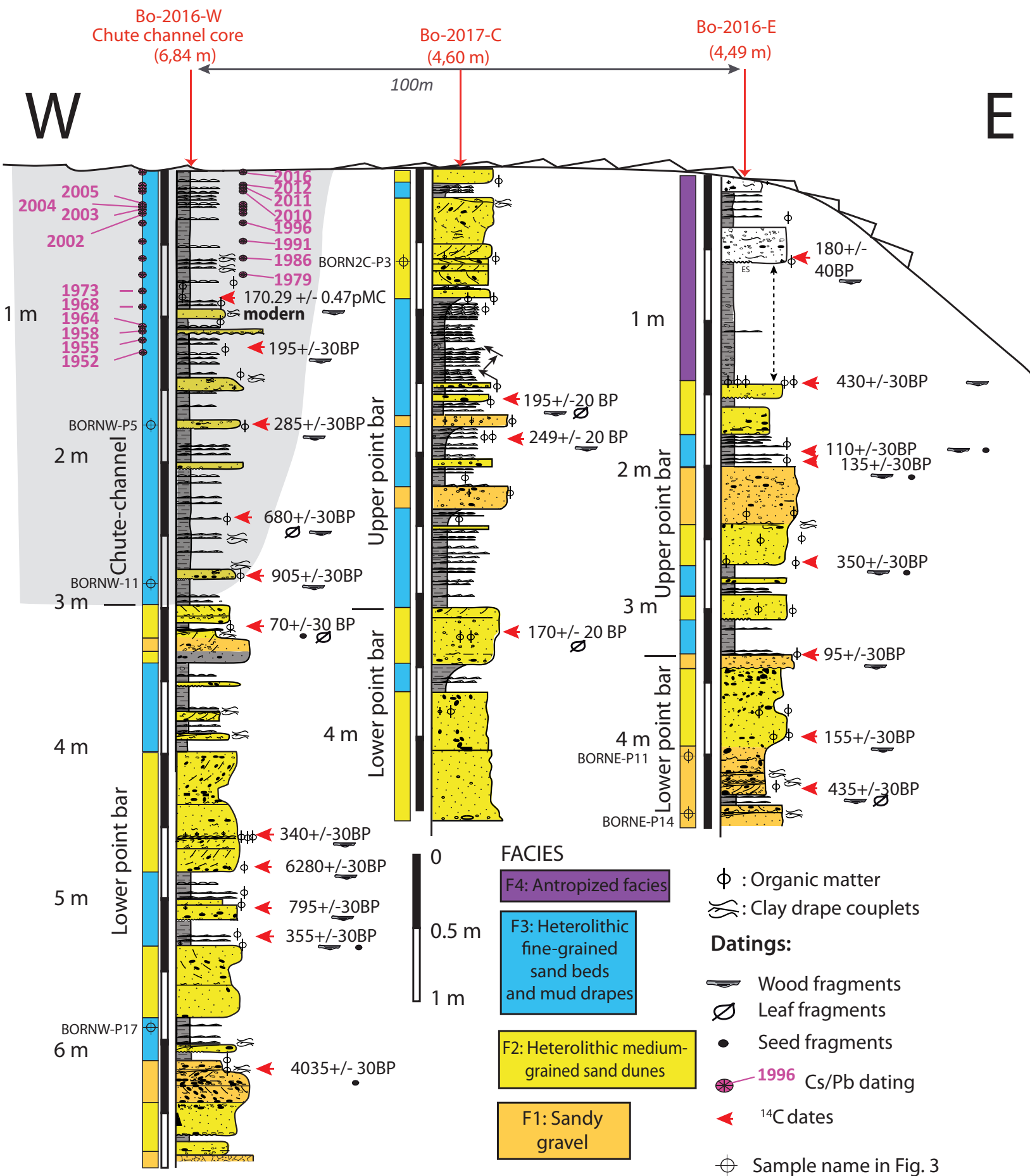


Figure 5

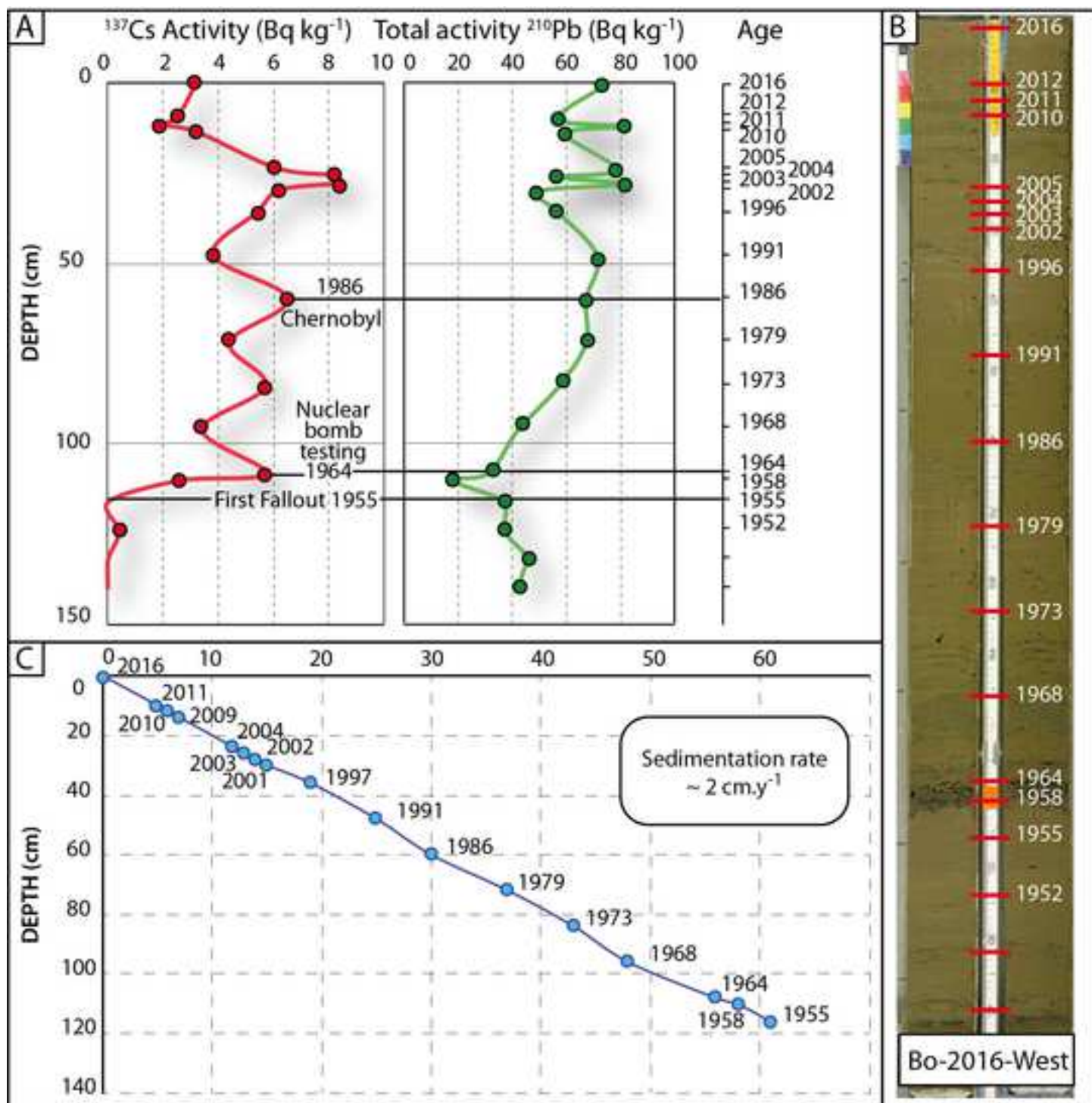
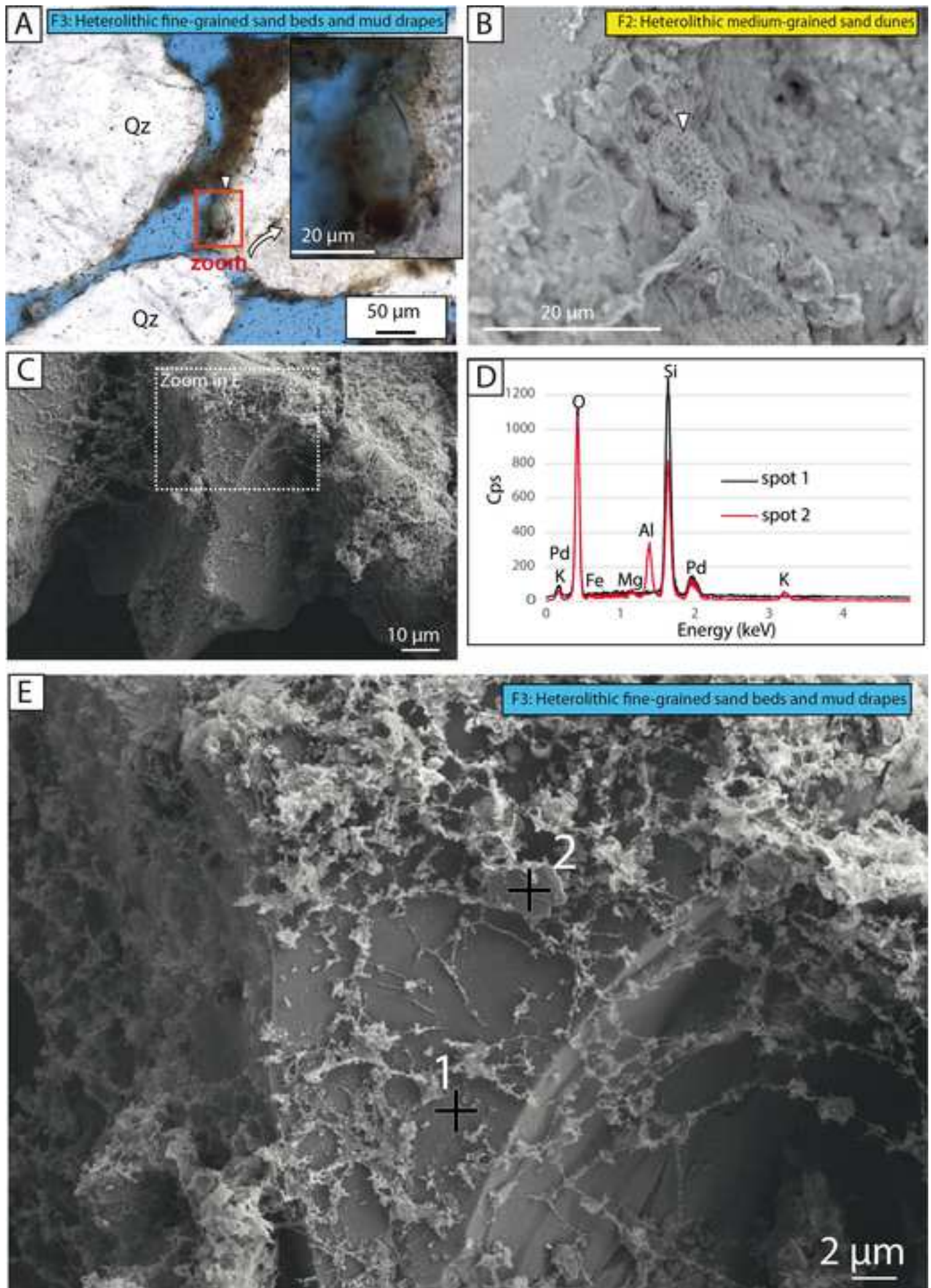
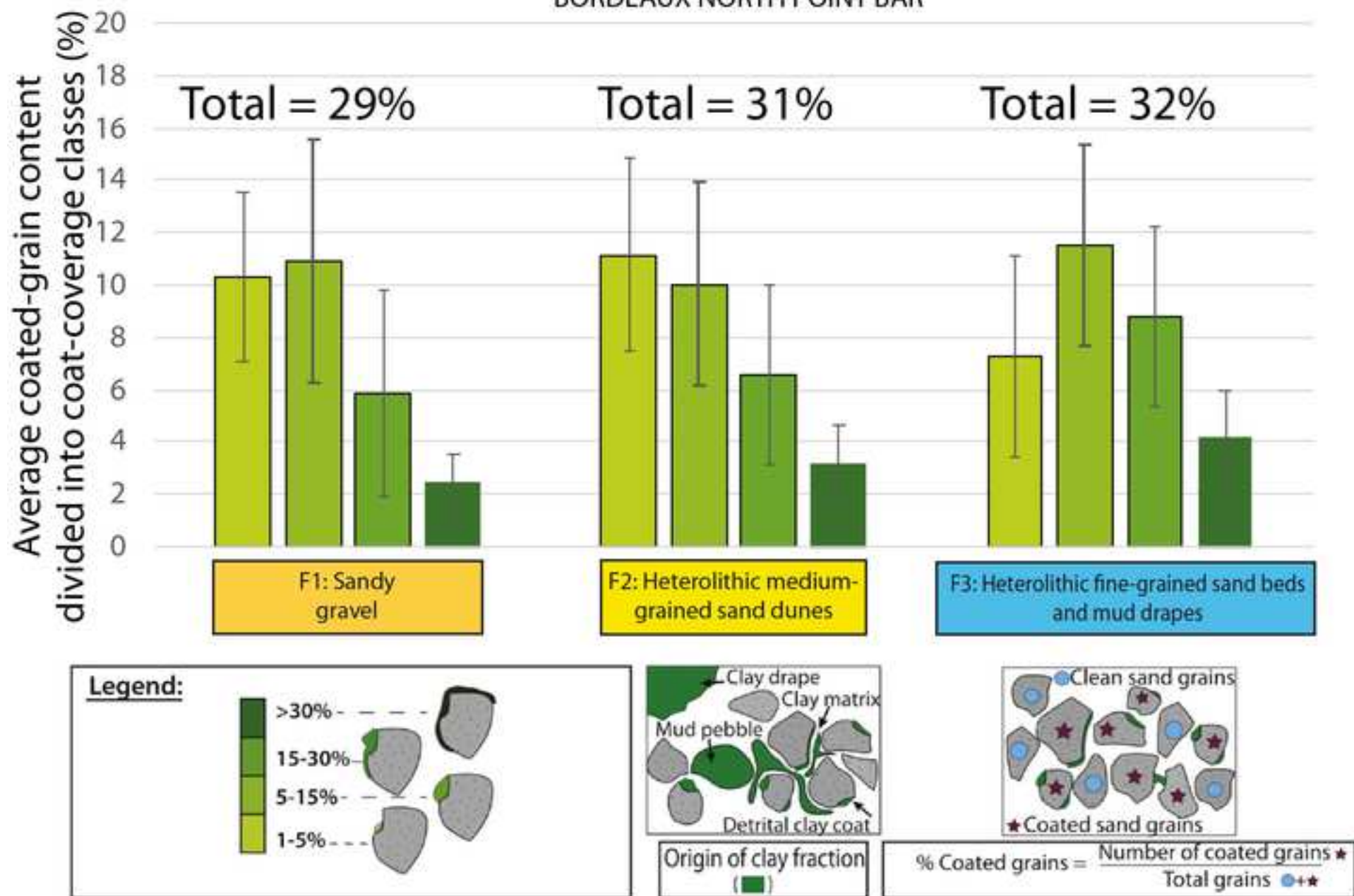
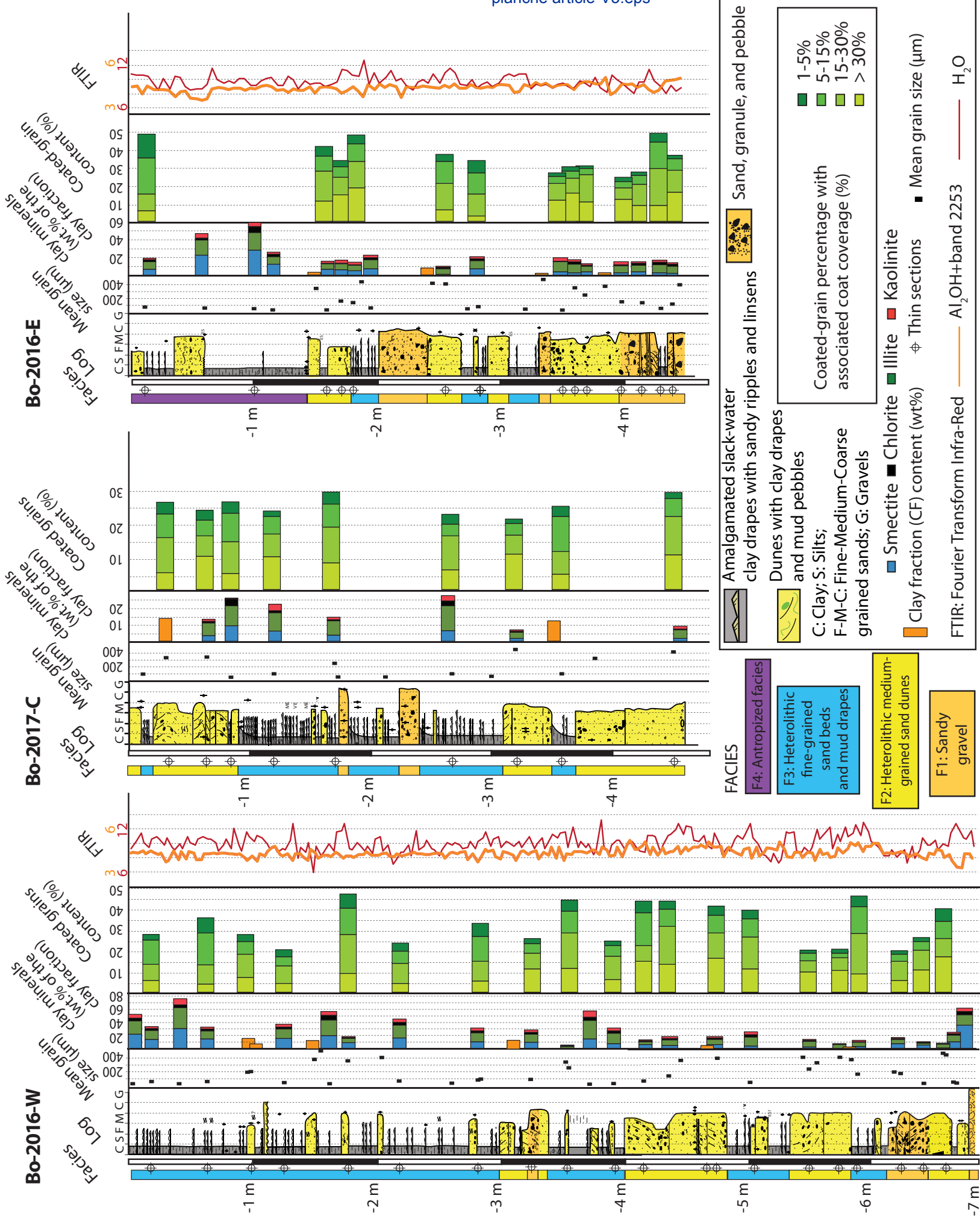


Figure 6



BORDEAUX NORTH POINT BAR





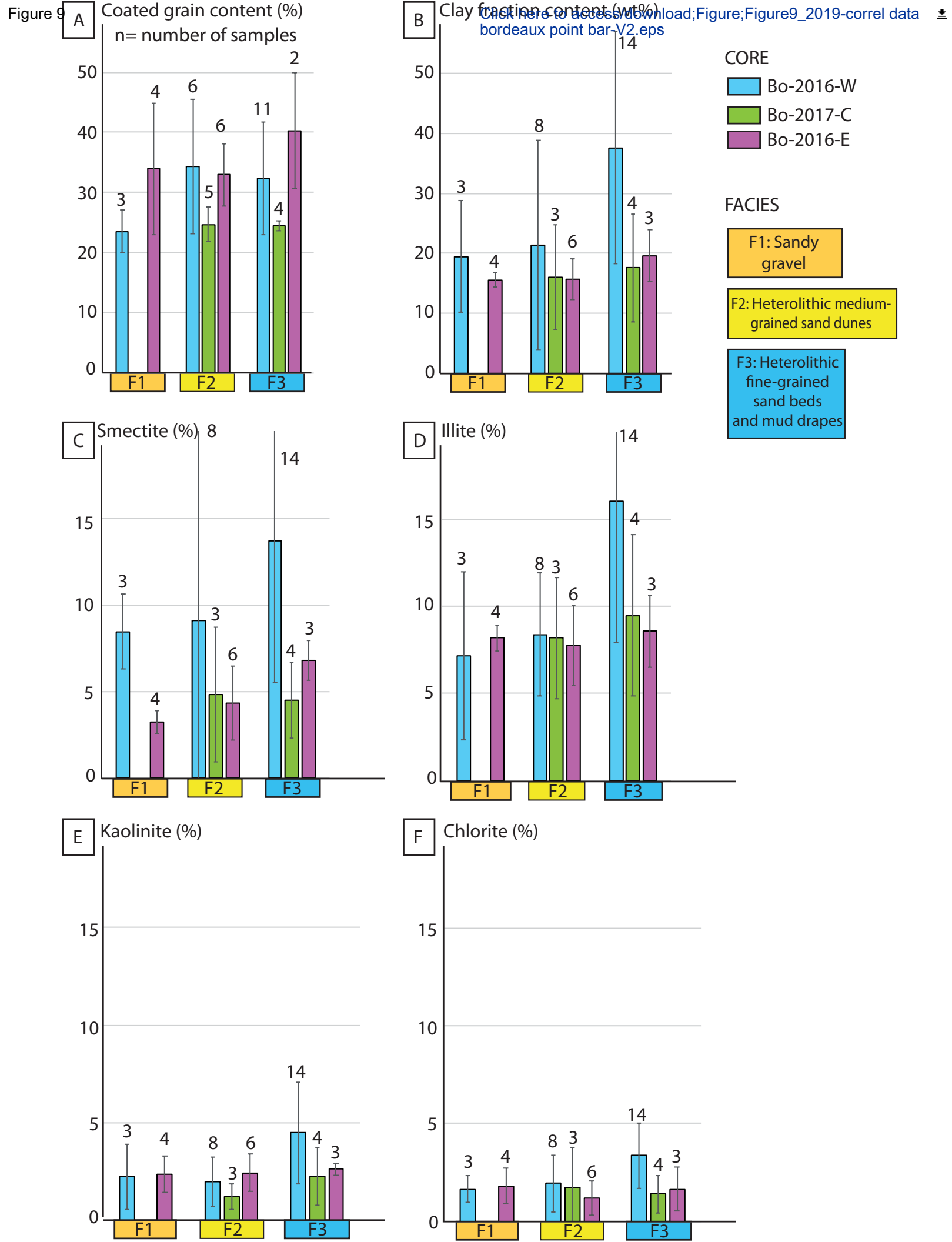
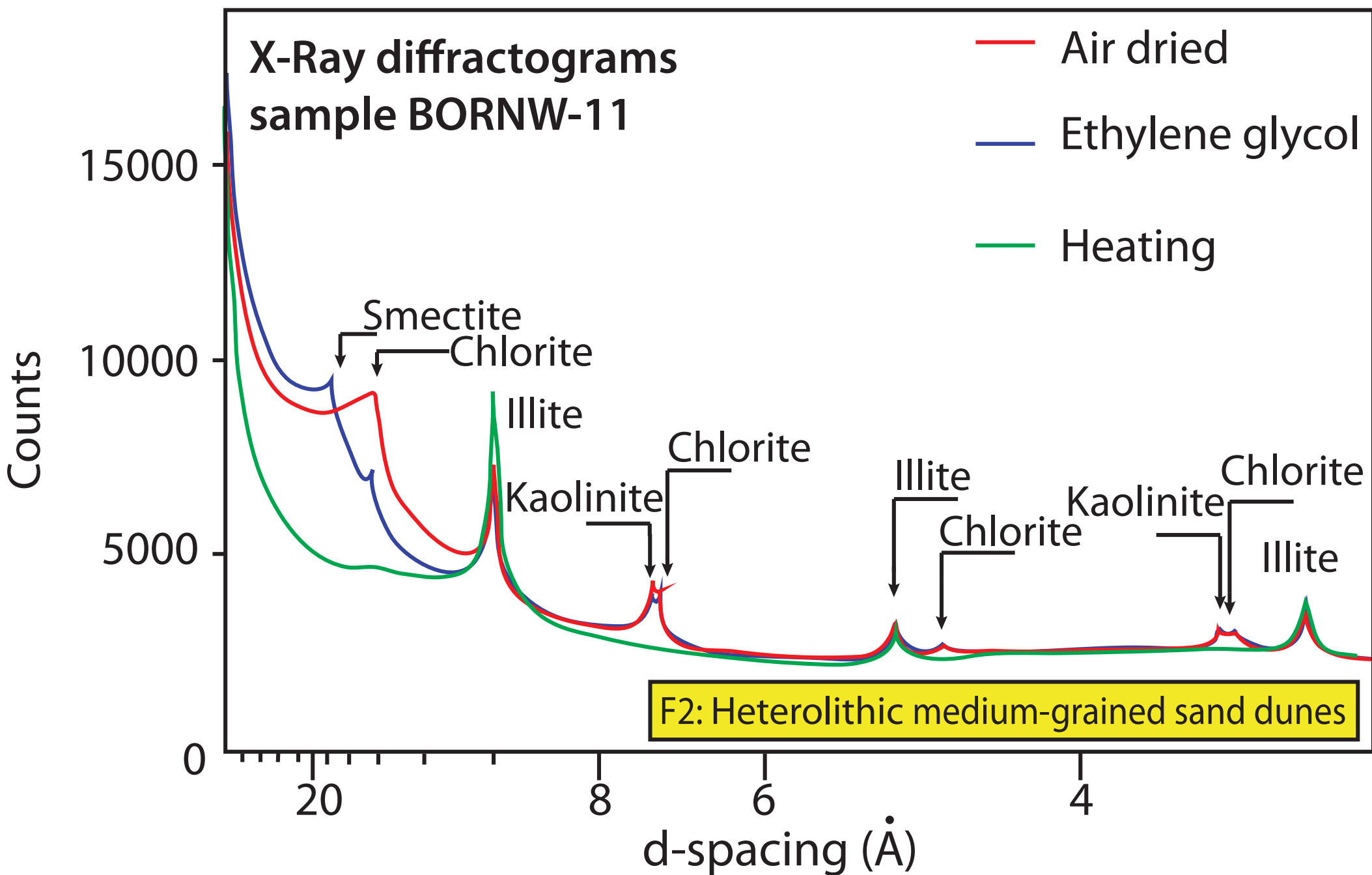
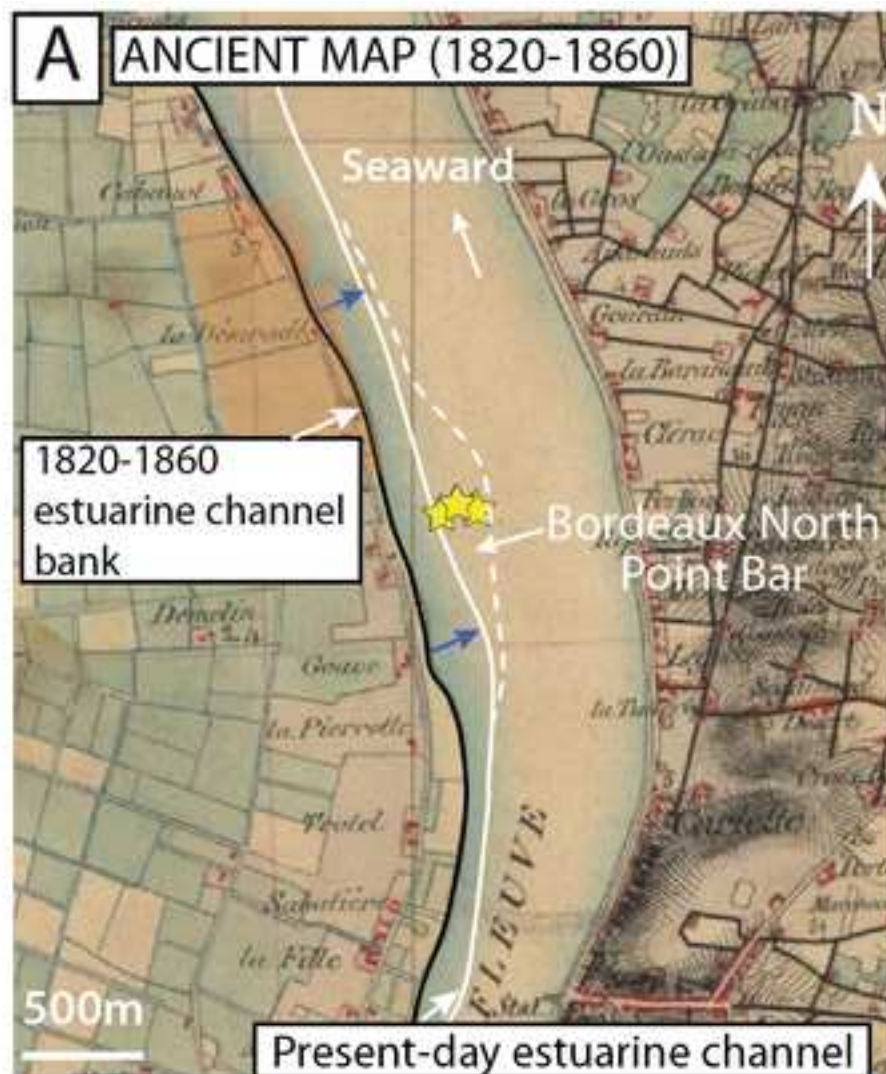
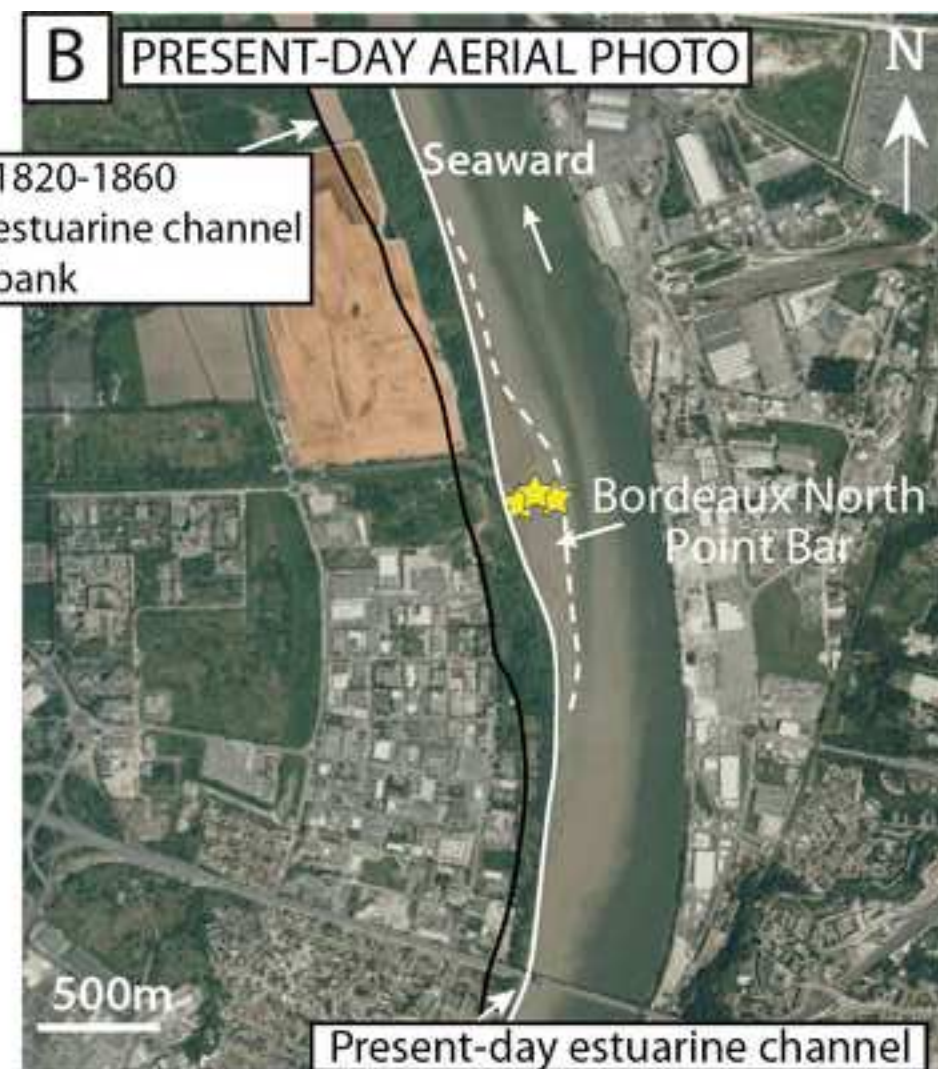


Figure 10

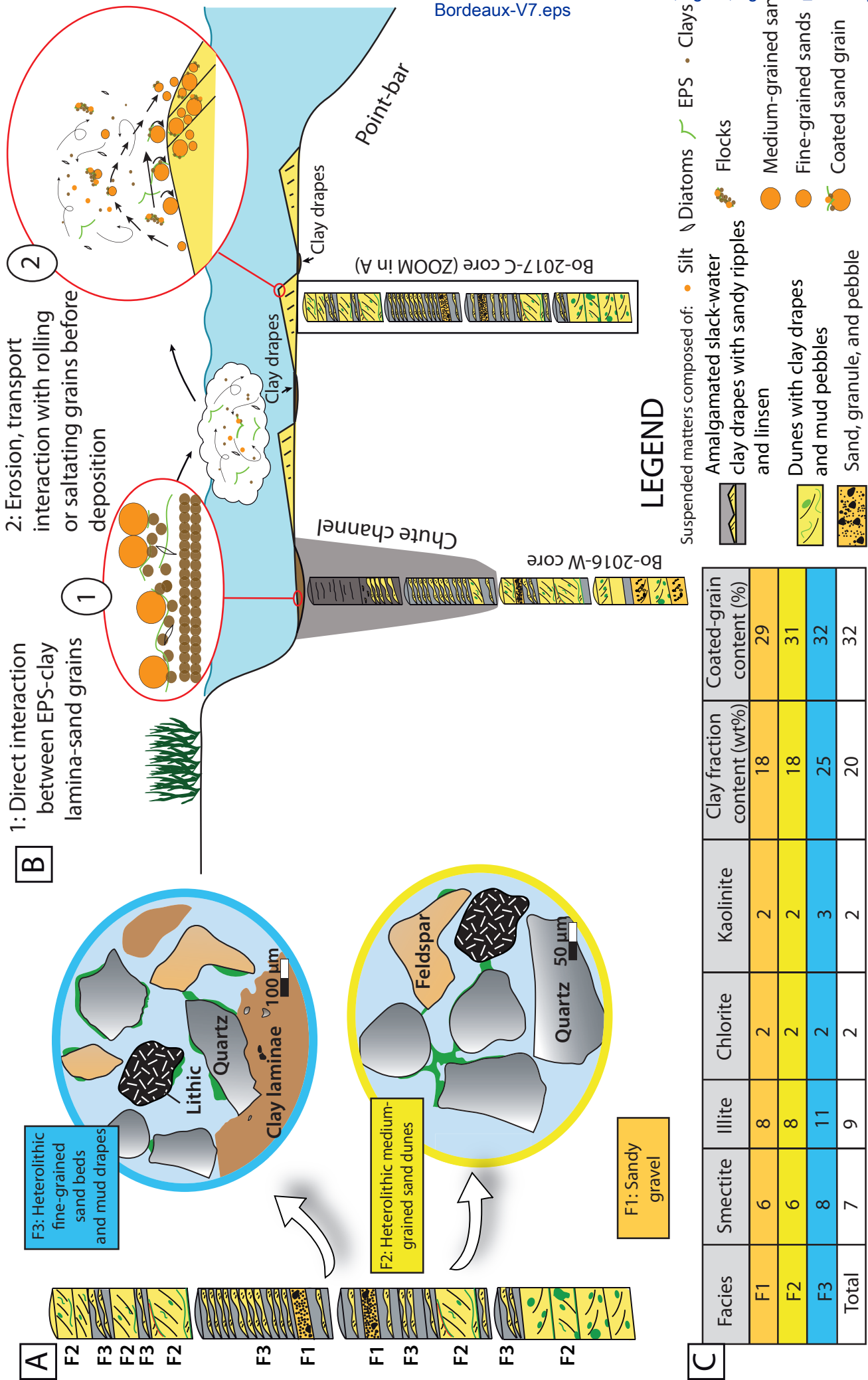




→ Lateral bank accretion
→ from the 19th century
(about 200 m)



★ Studied cores



Facies number	Facies name	Facies description	Texture	Thickness	Set thickness	Location in the bar
F1	Sandy gravel	Coarse-grained sands, pebbles, gravels with no sedimentary structures. It contains shells and shell fragments and mud clasts, wood, seed, or leaf debris.	Mean grain size: 209 μm . Grains are mostly subrounded and poorly sorted	At least centimeter thick, decimeter thick	/	Lower part
F2	Heterolithic medium-grained sand dunes	Sands with 5–30% clayey interbeds Small- to medium-size sand-rich dunes with few coarse mud pebbles on foresets and bottomsets or with thin clay drapes on foresets and bottomsets. Mud pebbles subrounded to subangular. Bottomsets are sometimes composed of thick individual horizontal clay drapes or thick amalgamated clay drapes. Some counter reactivation surfaces and clay drapes couplets are preserved. No bioturbation	Mean grain size: 266 μm . Grains are subrounded to subangular and moderately well sorted to poorly sorted	Decimeter to meter thick	Mean thickness of 12 cm	Lower part
F3	Heterolithic fine-grained sand beds and mud drapes	Clays with 10–30% sand interbeds Centimeter-to-decimeter-thick mud layers or centimetre-thick clay drapes alternating with sandy ripples, sandy to silty linsens, and rare small sand dunes with clay drapes on foresets and bottomsets. Mud layers may sometimes correspond to stacked amalgamated clay drapes. Neap-spring cycle may be recorded in this facies with millimetric alternations of thinly-bedded fine-grained silty linsen to centimeter-thick ripples with amalgamated clay drapes. Rare bioturbation observed (<i>Planolites</i> sp.?)	Mean grain size: 138 μm . Grains are subrounded to subangular and moderately well sorted	Decimeter to meter thick		Upper part
F4	Admixed and anthropized sand and mud facies	Mud-dominated facies composed of a mix of highly disturbed and anthropized sand and mud with many elements left by humans such as pieces of brick or shipyard bolts. Coarse-grained sand sometimes mixed within mud	Mean grain size: 69 μm	Meter thick	/	

Table 1

Facies	Grain composition - JmicroVision Image analysis on thin sections							Coated-grain content and coat coverage classes (percentage of the outer surface coated) - JmicroVision Image analysis on thin sections					Clay-fraction content - relative weight percentage of the clay fraction of homogenized sediment	Compositions of the clay fraction (< 2 μm) - X-ray diffraction (XRD)			
	Quartz (%)	Feldspars (%)	Lithic grains (%)	Carbonates (%)	Clays (%)	Macroporosity (%)	Micas (%)	1-5%	5-15%	15-30%	> 30%	Total coated grains (%)	Clay-fraction content (wt%)	% Smectite	% Illite	% Chlorite	% Kaolinite
F1	38	10	14	5	15	13	5	10	11	6	2	29	18	6	8	2	2
F2	39	12	14	2	13	14	5	11	10	7	3	31	18	6	8	2	2
F3	34	10	14	3	23	13	5	7	12	9	4	32	25	8	11	2	3
Total/Mean	37	11	14	3	17	13	5	10	11	7	3	31	20	7	9	2	2

Table 2

Depth		²¹⁰ Pb						¹³⁷ Cs	
cm	g cm ⁻²	Total	Unsupported		Supported			Bq kg ⁻¹	±
		Bq kg ⁻¹	±	Bq kg ⁻¹	±	Bq kg ⁻¹			
0.5	0.5	74.2	6	38.2	6.2	36	1.4	3.2	0.7
10	9.8	56.8	3.8	18	3.9	38.8	0.9	2.5	0.5
12	12.2	81.3	5.6	5.8	5.8	75.5	1.5	1.9	0.7
14	14.3	59.7	3.5	17.2	3.6	42.5	0.8	3.2	0.4
24	25.3	78.3	6.3	25.6	6.5	52.7	1.5	6.1	0.8
26	27.1	56.6	4.8	12	4.9	44.6	1.2	8.2	0.8
28	28.8	81.7	7	32.5	7.2	49.2	1.6	8.4	0.9
30	30.6	49.7	5.5	10.6	5.6	39.1	1.3	6.2	0.7
36	37.8	57.3	5.6	11.8	5.8	45.5	1.3	5.4	0.9
48	50	71.4	6.9	22.8	7.1	48.6	1.7	3.8	0.8
60	60.8	67.2	6.8	22.9	7	44.3	1.7	6.5	1.1
72	74.9	67.2	5.9	22.5	6	44.7	1.4	4.4	0.8
84	86.6	57.1	5.8	8.7	6	48.4	1.5	5.7	0.9
96	98.6	42.1	4.5	5.3	4.6	36.7	1.1	3.4	0.7
108	114	31.2	3.8	-0.7	3.9	31.9	0.9	5.7	0.6
110	117.2	17.9	2.3	1.5	2.4	16.3	0.6	2.6	0.4
116	123.3	36.9	4.2	0.4	4.3	36.5	1.1	0	0
124	131.3	37	5.1	-2.2	5.3	39.3	1.3	0.4	0.8
132	141.3	45.8	4.2	8	4.3	37.8	1	0	0
140	150.8	42.7	3.9	5.5	4	37.2	0.9	0	0
234	277.6	42.9	4.1	3.9	4.2	39	1	0.4	0.5

CLAY MINERALOGY X-RAY DIFFRACTOMETER

Sample		Facies	% Clay	% Smectite	% Illite
CORE Bo-2016-West					
Bdx-West-GR-1	100 cm	F3			
Bdx-West-GR-2	148 cm	F3			
Bdx-West-GR-3	205 cm	F3			
Bdx-West-GR-4	283 cm	F3			
Bdx-West-GR-5	310 cm	F2			
Bdx-West-GR-6	357 cm	F3			
Bdx-West-GR-7	445 cm	F2			
Bdx-West-GR-8	475 cm	F2			
Bdx-West-GR-9	545 cm	F2			
Bdx-West-GR-10	585 cm	F2			
Bdx-West-GR-11	623 cm	F1			
Bdx-West-GR-12	660 cm	F2			
BORNW-01	2 cm	F3	53	23	20
BORNW-02	18 cm	F3	34	15	14
BORNW-03	41 cm	F3	77	32	32
BORNW-04	63 cm	F3	34	15	12
BORNW-05	97 cm	F3			
BORNW-06	127 cm	F3	38	16	15
BORNW-07	161 cm	F3	57	21	24
BORNW-08	179 cm	F3	19	10	7
BORNW-09	218 cm	F3	46	17	20
BORNW-10	260 cm	F3			
BORNW-11	281 cm	F3	32	11	14
BORNW-12	323 cm	F1	29	11	12
BORNW-13	359 cm	F3	6	1	3
BORNW-14	371 cm	F3	58	15	28
BORNW-15	390 cm	F3	32	8	16
BORNW-16	415 cm	F2	14	7	5
BORNW-17	435 cm	F2	19	5	9
BORNW-18	471 cm	F2	19	6	8
BORNW-19	504 cm	F3	26	5	14
BORNW-20	550 cm	F2	15	3	8
BORNW-21	575 cm	F2	8	1	5
BORNW-22	590 cm	F3	13	4	7
BORNW-23	625 cm	F1	18	9	6
BORNW-24	645 cm	F1	11	6	3
BORNW-25	661 cm	F2	9	2	6
BORNW-26	666 cm	F2	25	11	10
BORNW-27	675 cm	F2	62	37	16
CORE Bo-2017-Center					
BORN2C-GR-1	31 cm	F2			
BORN2C-GR-2	64 cm	F2			
BORN2C-GR-3	170 cm	F3			

BORN2C-GR-4	320 cm	F2			
BORN2C-GR-5	385 cm	F2			
BORN2C-GR-6	450 cm	F2			
BORNC-01	11 cm	F3			
BORN2C-02	84 cm	F2	13	4	7
BORN2C-03	90 cm	F2	26	9	12
BORN2C-04	120 cm	F3	22	6	11
BORN2C-05	170 cm	F3	14	4	8
BORN2C-06	267 cm	F3	27	6	15
BORN2C-07	320 cm	F3	7	2	4
BORN2C-08	450 cm	F2	9	2	5
CORE Bo-2016-East					
Bdx-est-GR-1	150 cm	F2			
Bdx-est-GR-2	185 cm	F3			
Bdx-est-GR-3	245 cm	F1			
Bdx-est-GR-4	335 cm	F1			
Bdx-est-GR-5	385 cm	F2			
Bdx-est-GR-6	444 cm	F1			
BORNE-01	11 cm	F4	20	7	8
BORNE-02	58 cm	F4	47	23	17
BORNE-03	100 cm	F4	60	28	20
BORNE-04	115 cm	F4	26	13	8
BORNE-05	160 cm	F2	16	7	6
BORNE-06	170 cm	F2	17	7	7
BORNE-07	180 cm	F3	15	5	6
BORNE-08	195 cm	F3	23	8	10
BORNE-09	255 cm	F2	10	1	6
BORNE-10	273 cm	F3			
BORNE-11	281 cm	F3	21	7	9
BORNE-12	320 cm	F3			
BORNE-13	350 cm	F2	20	4	11
BORNE-14	360 cm	F2	18	3	10
BORNE-15	368 cm	F2	13	4	6
BORNE-16	400 cm	F1	16	3	8
BORNE-17	415 cm	F1	15	4	8
BORNE-18	430 cm	F1	17	3	9
BORNE-19	438 cm	F1	14	3	8

IMAGE ANALYSIS ON THIN SECTION					
			Quartz	Feldspars	Lithic

CORE Bo-2016-West

BORNW1-P-1	18 cm	F3	26	12	10
BORNW1-P-2	63 cm	F3	30	11	14
BORNW1-P-3	97 cm	F3	34	12	19
BORNW1-P-4	127 cm	F3	21	11	14
BORNW1-P-5	179 cm	F3	40	11	15

BORNW1-P-6	218 cm	F3	25	7	10
BORNW1-P-7	281 cm	F3	32	8	11
BORNW1-P-8	323 cm	F1	33	9	10
BORNW1-P-9	359 cm	F3	37	11	21
BORNW1-P-10	390 cm	F3	29	9	14
BORNW1-P-11	415 cm	F2	33	15	19
BORNW1-P-12	435 cm	F2	33	17	21
BORNW1-P-13	471 cm	F2	42	15	8
BORNW1-P-14	504 cm	F3	41	8	10
BORNW1-P-15	550 cm	F2	46	9	15
BORNW1-P-16	575 cm	F2	43	13	12
BORNW1-P-17	590 cm	F3	40	15	12
BORNW1-P-18	625 cm	F1	42	9	8
BORNW1-P-19	645 cm	F1	40	9	24
BORNW1-P-20	661 cm	F2	48	11	11
CORE Bo-2017-Center					
BORN2C-P1	31 cm	F2	37	13	15
BORN2C-P2	64 cm	F2	42	10	15
BORN2C-P3	84 cm	F2	34	10	10
BORN2C-P4	120 cm	F3	29	9	15
BORN2C-P5	170 cm	F3	40	12	13
BORN2C-P6	267 cm	F3	34	9	10
BORN2C-P7	320 cm	F2	44	16	13
BORN2C-P8	358 cm	F3	36	7	14
BORN2C-P9	450 cm	F2	41	17	13
CORE Bo-2016-East					
BORNE1-P-1	100 cm	F4	41	11	12
BORNE1-P-3	160 cm	F2	35	13	17
BORNE1-P-4	170 cm	F2	39	7	14
BORNE1-P-5	180 cm	F3	49	7	12
BORNE1-P-6	255 cm	F2	42	10	11
BORNE1-P-7	281 cm	F3	36	8	18
BORNE1-P-8	350 cm	F2	32	10	14
BORNE1-P-9	360 cm	F2	35	7	16
BORNE1-P-10	368 cm	F2	42	12	12
BORNE1-P-11	400 cm	F1	35	10	9
BORNE1-P-12	415 cm	F1	45	9	10
BORNE1-P-13	430 cm	F1	38	14	17
BORNE1-P-14	438 cm	F1	35	11	20

% Chlorite	% Kaolinite	mean grain size
------------	-------------	-----------------

		201
		394
		411
		98
		349
		325
		370
		397
		408
		383
		192
		461
4	6	38
3	3	74
4	9	36
3	3	76
		199
3	4	52
7	6	35
2	1	365
4	5	74
		47
3	4	93
2	4	92
1	1	270
5	9	35
3	5	38
1	2	78
2	3	138
2	2	74
4	4	51
2	1	244
1	1	402
1	2	161
2	2	179
1	1	41
1	1	443
2	2	47
5	4	31
		334
		346
		248

		462
		342
		422
		101
1	1	56
4	1	102
1	4	71
1	1	56
3	3	105
1	1	74
0	2	91
		342
		447
		427
		492
		379
		399
2	2	89
2	5	75
7	5	61
3	2	50
1	2	43
0	3	168
0	3	126
3	3	68
2	1	414
		57
2	2	85
		51
1	4	49
3	2	360
1	2	253
1	4	159
2	2	142
3	2	56
2	2	120

CaCO3	Clays	Porosity	Others	Coated grains		
				1-5%	5-15%	15-30%

2	32	16	3	6	8	11
2	33	7	4	4	9	15
5	14	12	5	7	11	6
4	37	10	3	4	8	4
0	17	11	5	9	18	12

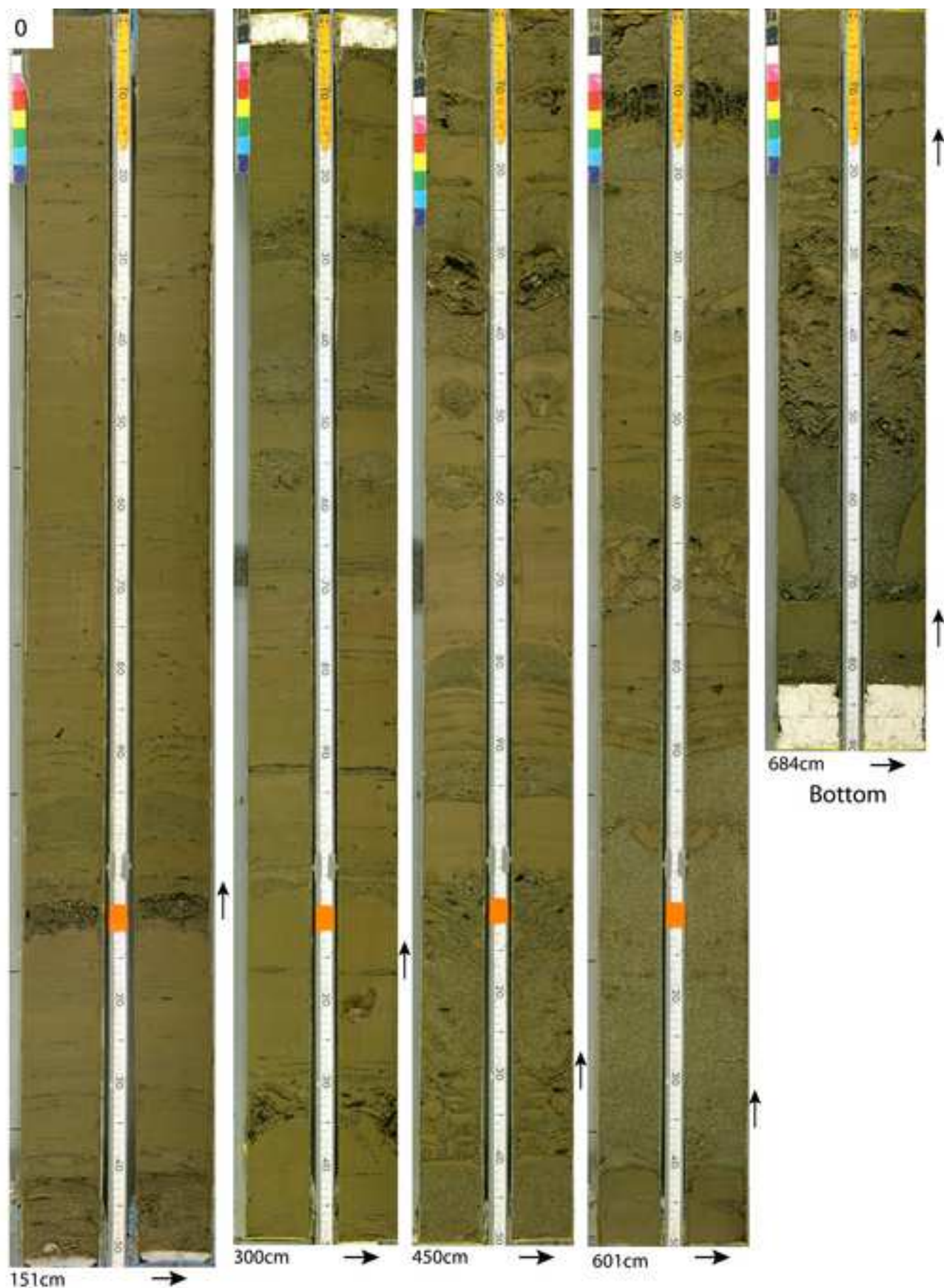
2	46	7	4	4	10	6
2	31	14	3	5	9	12
2	29	13	3	11	7	4
3	6	17	5	11	17	10
4	31	6	7	6	11	5
1	9	19	4	15	7	16
0	13	12	4	13	18	8
1	18	13	3	16	12	8
3	26	8	4	11	15	9
1	10	16	2	10	5	4
2	8	16	5	10	6	2
1	12	13	7	9	19	13
3	17	14	7	5	9	3
3	8	9	7	10	9	4
3	9	11	6	17	8	8
3	12	15	5	5	10	7
3	10	15	5	10	6	5
2	25	15	4	5	9	8
4	22	17	4	10	7	5
5	14	13	4	8	10	7
1	27	16	3	6	10	3
1	7	15	4	10	6	3
4	17	16	6	4	7	10
1	8	14	6	10	11	5
2	18	13	4	6	9	20
3	15	12	4	11	16	8
2	17	14	8	15	9	6
1	15	13	4	18	15	10
4	10	19	4	6	15	12
1	10	20	7	3	12	12
4	19	15	7	12	9	4
3	14	17	7	15	8	4
6	13	9	5	11	15	4
8	15	18	5	12	6	4
5	14	12	4	9	12	5
2	14	9	5	9	20	15
8	8	13	5	16	12	6

--

> 30%	Total coated grain content
-------	----------------------------

2	27
7	35
3	27
3	20
7	46

4	23
6	32
2	25
5	43
2	24
5	43
4	43
4	40
4	39
1	20
2	20
5	45
2	19
2	26
6	39
3	25
3	23
3	26
2	23
3	29
3	22
1	21
3	24
2	28
13	48
5	41
3	33
5	47
4	36
7	33
2	26
3	30
1	30
2	24
2	27
5	48
2	36

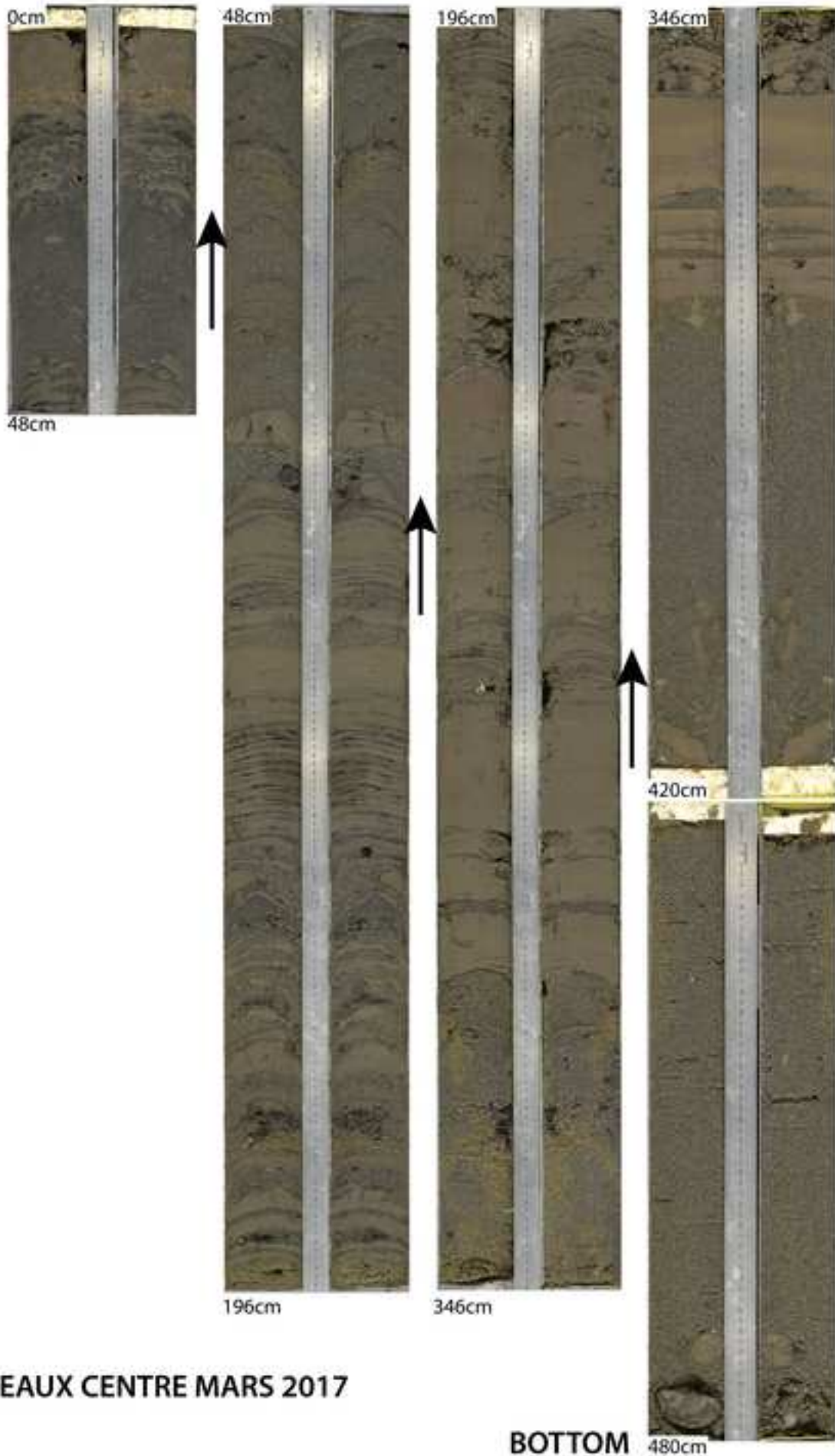


Point bar of Boreaux Nord, West part (chute channel)

Downstream marked by the arrows

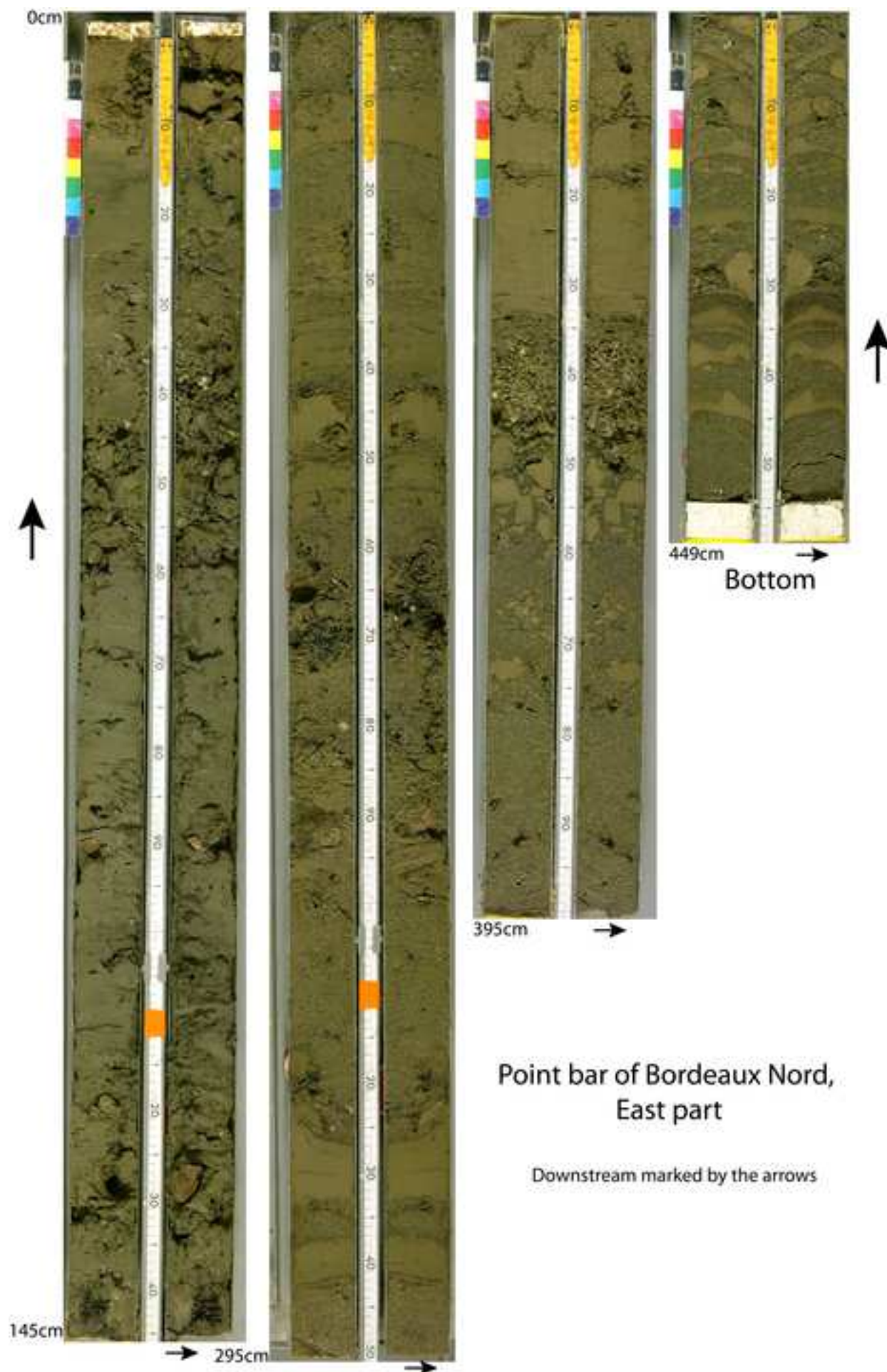


TOP



BORDEAUX CENTRE MARS 2017

BOTTOM



Point bar of Bordeaux Nord,
East part

